

RESEARCH

Open Access



Imaging flow cytometry-based cellular screening elucidates pathophysiology in individuals with Variants of Uncertain Significance

Irena Josephina Johanna Muffels^{1*} , Hans R. Waterham^{2,3}, Giuseppina D'Alessandro⁴, Guido Zagnoli-Vieira⁵, Michael Sacher^{6,7}, Dirk J. Lefeber⁸, Celine Van der Vinne¹, Chaim M. Roifman⁹, Koen L. I. Gassen¹⁰, Holger Rehmann¹¹, Desiree Y. Van Haften-Visser¹², Edward S. S. Nieuwenhuis^{1,13}, Stephen P. Jackson⁴, Sabine A. Fuchs^{1†}, Femke Wijk^{14†} and Peter van Hasselt^{1*}

Abstract

Background Deciphering variants of uncertain significance (VUS) represents a major diagnostic challenge, partially due to the lack of easy-to-use and versatile cellular readouts that aid the interpretation of pathogenicity and pathophysiology. To address this challenge, we propose a high-throughput screening of cellular functionality through an imaging flow cytometry (IFC)-based platform.

Methods Six assays to evaluate autophagic-, lysosomal-, Golgi- health, mitochondrial function, ER stress, and NF- κ B activity were developed in fibroblasts. Assay sensitivity was verified with compounds ($N=5$) and positive control patients ($N=6$). Eight healthy controls and 20 individuals with VUS were screened.

Results All molecular compounds and positive controls showed significant changes on their cognate assays, confirming assay sensitivity. Simultaneous screening of positive control patients on all six assays revealed distinct phenotypic profiles. In addition, individuals with VUS(es) in well-known disease genes showed distinct – but similar—phenotypic profiles compared to patients with pathogenic variants in the same gene.. For all individuals with VUSes in Genes of Uncertain Significance (GUS), we found one or more of six assays were significantly altered. Broadening the screening to an untargeted approach led to the identification of two clusters that allowed for the recognition of altered cell cycle dynamics and DNA damage repair defects. Experimental follow-up of the ‘DNA damage repair defect cluster’ led to the discovery of highly specific defects in top2cc release from double-strand DNA breaks in one of these individuals, harboring a VUS in the *RAD54L2* gene.

[†]S. A. Fuchs and F. Wijk contributed equally to this work.

*Correspondence:

Irena Josephina Johanna Muffels

i.j.j.muffels-2@umcutrecht.nl

Peter van Hasselt

p.vanhasselt@umcutrecht.nl

Full list of author information is available at the end of the article



© The Author(s) 2025. **Open Access** This article is licensed under a Creative Commons Attribution-NonCommercial-NoDerivatives 4.0 International License, which permits any non-commercial use, sharing, distribution and reproduction in any medium or format, as long as you give appropriate credit to the original author(s) and the source, provide a link to the Creative Commons licence, and indicate if you modified the licensed material. You do not have permission under this licence to share adapted material derived from this article or parts of it. The images or other third party material in this article are included in the article's Creative Commons licence, unless indicated otherwise in a credit line to the material. If material is not included in the article's Creative Commons licence and your intended use is not permitted by statutory regulation or exceeds the permitted use, you will need to obtain permission directly from the copyright holder. To view a copy of this licence, visit <http://creativecommons.org/licenses/by-nc-nd/4.0/>.

Conclusions Our high-throughput IFC-based platform simplifies the process of identifying VUS pathogenicity through six assays and allows for the recognition of useful pathophysiological markers that structure follow-up experiments, thereby representing a novel valuable tool for precise functional diagnostics in genomics.

Keywords Imaging flow cytometry, Variant of uncertain significance, Precision genomic diagnostics, DNA damage repair defect, Genetic diseases, Metabolic disorders, High-throughput screening, Functional genomics

Background

The “genetics first” era has revolutionized the diagnostics of genetic disease. In its slipstream, genetic screening has offered hints for yet uncharacterized disease entities: Variants of uncertain significance (VUS). For these variants, a connection to human disease has yet to be established. Elucidating the significance of a VUS is painstakingly complex, as it requires *in silico*, *in vitro*, *in vivo*, and expert human analyses. It may take years to study the functional impact of a genetic variant on RNA levels, protein levels, and cellular pathways, and at significant costs, whereas the outcome of this endeavor is uncertain [1]. As a consequence, many VUS cases are left unexplored and unsolved. For patients, the absence of a diagnosis hampers prognosis prediction, family counseling, and treatment allocation, resulting in significant morbidity and mortality [2].

A key aspect of elucidating VUS pathology is determining the impact of the variant on cellular function. Beyond the effects of a VUS on RNA- or protein stability, it is imperative to assess which intracellular pathways are affected by the variant. However, it can be highly challenging to decide which of the numerous potentially affected cellular pathways should be studied first, and which assays should be prioritized. Nonetheless, pathway-based functional insights are crucial to unravel disease pathophysiology in relation to the clinical phenotype and to develop effective therapeutic strategies. We hypothesized that screening for morphological and functional cellular changes could reduce the time that is needed to design effective functional assays that help delineate the main factor(s) at play. By narrowing down the cellular pathways that could be studied, a functional cellular screening could provide a starting point to allow a more targeted set-up of subsequent experimental follow-up assays.

Microscopy has become increasingly popular to screen for cellular dysfunction in human diseases [3]. The largest benefit of microscopic screening is the fact that prior knowledge about underlying pathophysiology is not required, circumventing the need for expert-craft cellular assays [4, 5]. However, this approach has not been tested for individuals with VUS on a larger scale, and additionally, untargeted microscopic screening comes with its own set of challenges, especially in regard to extracting

relevant phenotypic profiles. Imaging flow cytometry (IFC) combines flow cytometry with microscopy, and its high-throughput potential combined with a simple analysis tool allows rapid extraction of relevant features and morphological profiles, without the need for deep learning models or computational scripts. These aspects make IFC highly suitable for untargeted screening for individuals with VUS.

Here, we developed a novel screening platform to identify functional cellular aberrancies in individuals with VUS using imaging flow cytometry (IFC). We developed six assays to quantify morphology and function of six important cellular organelles and pathways (autophagy – Golgi – lysosomes – mitochondria – endoplasmic reticulum – NF- κ B). We confirmed all molecular compounds and positive control patients showed significant changes on cognate assays. Next, we screened 20 patients with VUS(es) in well-known disease genes ($N=7$) and VUS in GUSes (genes of uncertain significance) ($N=13$). For all individuals with VUS, we found significant changes on one or more IFC assays, which were validated using additional functional assays, thereby unveiling the IFC-based platform as a valuable tool for the detection of relevant pathophysiological mechanisms for individuals with VUS.

Methods

Ethics, consent and permission

All patients without diagnosis despite an extensive diagnostic workup, including whole exome sequencing seen at the outpatient clinic of the Department of Metabolic Diseases of the Wilhelmina Children’s Hospital in Utrecht, were eligible for inclusion in this study. The Wilhelmina Children’s Hospital is a tertiary center and provides specialized care for pediatric patients. For the 7 patients with VUS in well-known disease genes, we included all patients for which we could identify a positive control ($N=7$) counterpart in our biobank. For the cohort of VUS, 49 patients were eligible for inclusion. Since we only wanted to include patients that had fibroblasts obtained prior to this study for diagnostic purposes, 30 patients were excluded, since no material was stored for these patients. Of the 19 patients that were left, 2 were excluded since they were diagnosed within

the study period. Four patients were excluded since in-depth functional testing was performed for their specific VUS in other hospitals. All patients consented to use their residual material collected for diagnostic purposes in the Wilhelmina Children's Hospital metabolic biobank (TCBio 19–489/B and 22–284 (ImaVUS) <https://tcbio.umcutrecht.nl>). Six healthy controls were included through the same biobank. Fibroblasts of a patient with pathogenic *ERCC1* variants was provided by the Genome Damage and Stability Centre Research Tissue Bank (GDSC-RTB), University of Sussex [6]. Fibroblasts of a patient with pathogenic *TDP2* variants were provided by Dr. Zagnoli-Vieira [7]. The GDSC-RTB is approved by the Wales REC 3 to release human cell lines for research (19/WA/0091). All procedures performed in studies involving human participants were in accordance with the ethical standards of the institutional and/or national research committee(s) and with the Helsinki Declaration (as revised in 2013).

Whole exome sequencing

Genomic DNA was isolated from blood samples. The variants of the individuals were identified through trio Whole Exome Sequencing. Exomes were enriched using Agilent SureSelect XT Human All Exon kit V5 and sequenced on a HiSeq sequencing system (Illumina). Reads were aligned to hg19 using Burrows–Wheeler Aligner. Variants were called using Genome Analysis Toolkit Variant Caller and annotated, filtered. The minimal coverage of the full target was $>15 \times 99\%$ [8–11].

The sequencing data was processed with an in-house developed pipeline based on the Genome Analysis Toolkit (GATK v3.8–1-0-gf15c1c3ef) best practices guidelines [12, 13]. The read pairs were mapped with BWA-MEM v0.7.5a, marking duplicates and merging lanes using Sambamba v0.6.5 and realigning indels using GATK IndelRealigner [14, 15]. Next, the GATK Haplotypecaller was used to call single-nucleotide polymorphisms and indels, creating variant call formatted files.

Variants were annotated, filtered, and prioritized using the Alissa Interpret Clinical Informatics Platform (Platform dataset version 17, Agilent) following a validated filtering tree routinely used in our genome diagnostics center. Tree filtering criteria were that the variant be exonic or intronic within 20 base pairs of the exon boundary and a maximum allele frequency of 0.5% in the GnomAD database (version 3), consisting of $>140,000$ healthy controls [8]. At least one functional effect predictor should predict the variant to be “likely pathogenic” (PolyPhen2 HumDiv and HumVar prediction, SIFT score <0.05) and at least one of the conservation scores should predict high conservation, namely Grantham score >100 , GERP+ >2 , or PhyloP >2.5 [16–20]. All

laboratory processes were performed in our ISO15189 accredited diagnostic laboratory [21, 22]. Manual review involved the following stringent criteria: variants were excluded in case of synonymous variants, intronic variants with no predicted effect on splicing according to the Splice Prediction Module in Alamut Visual (Version 2.14), the variant being present in <10 reads and in case of a single variant being present in a heterozygous state in a known autosomal recessive disease gene [23]. Variants were assessed based on their GnomAD allele frequency, with the cut-off determined by the frequency of the disease in the associated population, i.e., the specific allele frequency could maximally explain 10% of all disease cases [8].

Fibroblast cultures

Fibroblasts had been obtained previously for diagnostic purposes, using forearm punch biopsies. Cells were cultured in fibroblast culture medium (HAM F12 with 10% fetal bovine serum, penicillin (100 UI/ml) and streptomycin (100 $\mu\text{g/ml}$)), in a humidified incubator at 37 °C and 5% CO₂. Medium was changed every 3–4 days. Cells were split at 80% confluency.

Clonogenic survival assays and stainings to detect γH2AX foci

For clonogenic assays, fibroblasts of healthy controls, patients with pathogenic *TDP2* variants, and the individual with RAD54L2 VUS were plated and treated 24 h later, and then stained and counted 14–21 days later, when visible colonies had formed. All clonogenics were carried out in 10-cm dishes containing a feeder layer of 5×10^4 fibroblasts irradiated with 35 Gy. Cells were treated with Etoposide (VP-16, Cayman Chemicals) for the indicated timeframes or irradiated with indicated doses using CellRAD (Faxitron). For imaging purposes, cells were plated in 24-well imaging plates, treated with Etoposide (30 μM , 30 min), washed, and released for the indicated period of time. After treatment, cells were fixed in 4% paraformaldehyde for 10 min, permeabilized in phosphate-buffered saline (PBS)–0.2% Tween for 10 min, and blocked in PBS–5% bovine serum albumin (BSA) for at least 30 min. After 1 h of incubation at room temperature with primary antibodies (γH2AX , Cell Signaling Technology, and cyclin A, BD Biosciences), cells were washed in PBS–0.2% Tween three times and incubated with secondary antibodies for 45 min. After three more washes in PBS–0.2% Tween, nuclei were stained with 4',6-diamidino-2-phenylindole for 10 min. Images were acquired and analyzed using the Opera Phenix microscope. All quantifications were done in cyclin A-negative cells representing G1 population.

Positive controls—molecular compounds

To validate the specificity of the assays and features used for this project, molecular compounds were used as positive controls. Healthy control fibroblast lines were incubated with 25 ng/ml ethidiumbromide (Sigma Aldrich) for 7 days to deplete mitochondrial mass and FCCP (TargetMol) for 5 min to abolish membrane potential (3 μ M). Bafalomycin (Sigma Aldrich) was added at 0.2 μ M for 8 h to stimulate autophagosome accumulation. For ER stress, cells were incubated with Brefeldin A (Bio Legend) for 16 h at a concentration of 10 μ g/ml. To induce NF- κ B translocation, cells were stimulated with TNF- α for 30 min at a concentration of 20 ng/ml. To induce Golgi fragmentation, cells were incubated with Nocodazole (Sigma Aldrich) for 16 h at a concentration of 0.3 μ M.

Imaging flow cytometry assays in fixed cells

For IFC analysis, cells were collected using Accutase (Stempro) and fixed immediately with fix/perm buffer (BD Biosciences). For the autophagy assay, cells were harvested, incubated in 0.5% saponin in PBS0 for 30 min, spun down, and fixed with 4% formaldehyde. For the NF- κ B assay, 4% formaldehyde was used instead of fix/perm buffer. Cells were stained using LAMP1 (Abcam), LC3B (MBL International), ATF6 (Novus Biologicals), GM130 (Abcam), p65 (Cell Signaling Technology), and DRAQ5 (Biolegend) in perm/wash buffer (BD Biosciences). For the NF- κ B assay, PBS0 with 1% FBS and 0.1% triton-X-100 was used instead of perm/wash buffer. For IFC analysis, cells were resuspended in 20 μ L of 1% FBS in PBS0 at a concentration of approximately 5000 cells/ μ L. The laser power of the 488 and 642 laser were adjusted to avoid saturation (pixel intensity < 1500) and consistent voltages were maintained throughout experiments. Cells were acquired using the $\times 60$ magnification and low speed fluidics using the MKII Imagestream with Inspire (Version 201.1.0.765, Cytex Biosciences). Cells with a raw nuclear pixel intensity (the sum of pixel intensity within the mask) $> 1 \times 10^5$ pixels were processed for downstream analyses.

Imaging flow cytometry assay in living cells (mitochondrial assay)

Cells were plated in 6-well plates to reach 70–80% confluency at the day of the assay. At the day of the assay, cells were incubated with the following antibodies TMRM (30 nM, Sigma Aldrich), NAO (50 nM, Enzo Life Sciences) and DRAQ5 (Biolegend) at 37° in HBSS for 40 min. FCCP (3 μ M, TargetMol) was added the last 5 min of incubation [24]. After incubation, cells were washed once with PBS0 and incubated with TrypLE (Gibco) for 2 min. Cells were harvested using 1 mL 10% dialyzed FBS (Gibco) in PBS0, spun down, resuspended

in small volumes (< 30 μ L) and immediately visualized using IFC. Since lipophilic cations like TMRM are extruded by multidrug resistance (MDR) transporters [25], TMRM fluorescence is not stable for prolonged periods [26]. Therefore, we included 4 samples per experiment (one healthy control and one patient, two samples per donor (with and without FCCP) and measured each sample for 2 min. This setup allowed us to perform each IFC experiment within 30 min after the initial staining procedure.

The laser power of the 488 and 642 laser were adjusted to avoid saturation (Raw median pixel intensity < 1500) and consistent voltages were maintained throughout experiments. Compensation files were created using single staining for all channels. Compensation settings were calculated using IDEAS software (Version 6.2, Cytex Biosciences). Cells were acquired using the $\times 60$ magnification and low speed fluidics using the MKII Imagestream with Inspire (Version 201.1.0.765, Cytex Biosciences). Cells with a raw nuclear pixel intensity (the sum of pixels within the mask) $> 1 \times 10^5$ pixels were processed for downstream analyses.

IFC data analysis—IDEAS

Data was analyzed using IDEAS software (Version 6.2, Cytex Biosciences). Gating strategy and masks used for each experiment can be found in Additional File 1: Figure S1. For each donor, > 200 cells were analyzed. For mitochondrial mass and membrane potential, median pixel intensity of the NAO and the TMRM staining, respectively, were extracted for each donor. Each patient was compared to one healthy control counterpart analyzed in the same experiment. For all other assays, patients were compared with at least three healthy controls. To quantify Golgi functionality, the percentage of cells with intact Golgi system was calculated. To quantify autophagy, the mean spot count was extracted. To quantify NF- κ B activity and ER stress, the percentage of cells with translocated p65/AF6 were compared between donors.

IFC data analysis in R

To create Fig. 1, raw feature values for single cells were extracted from IDEAS as excel files, and analyzed using R (Version 4.2.3) and R-studio (Version 2022.12.0.353). Before extraction of raw data, compensation was applied, and out of focus cells and doublets were removed using IDEAS. The boxplot in Fig. 1 shows the non-normalized feature values per cell per condition. For Figs. 2 and 3, similarity was calculated using Manhattan distance, and clustering was performed using average linkage clustering. Clustering performance was determined using the Elbow Method, by plotting the total intra-cluster variation (WSS) for each additional cluster. We configured

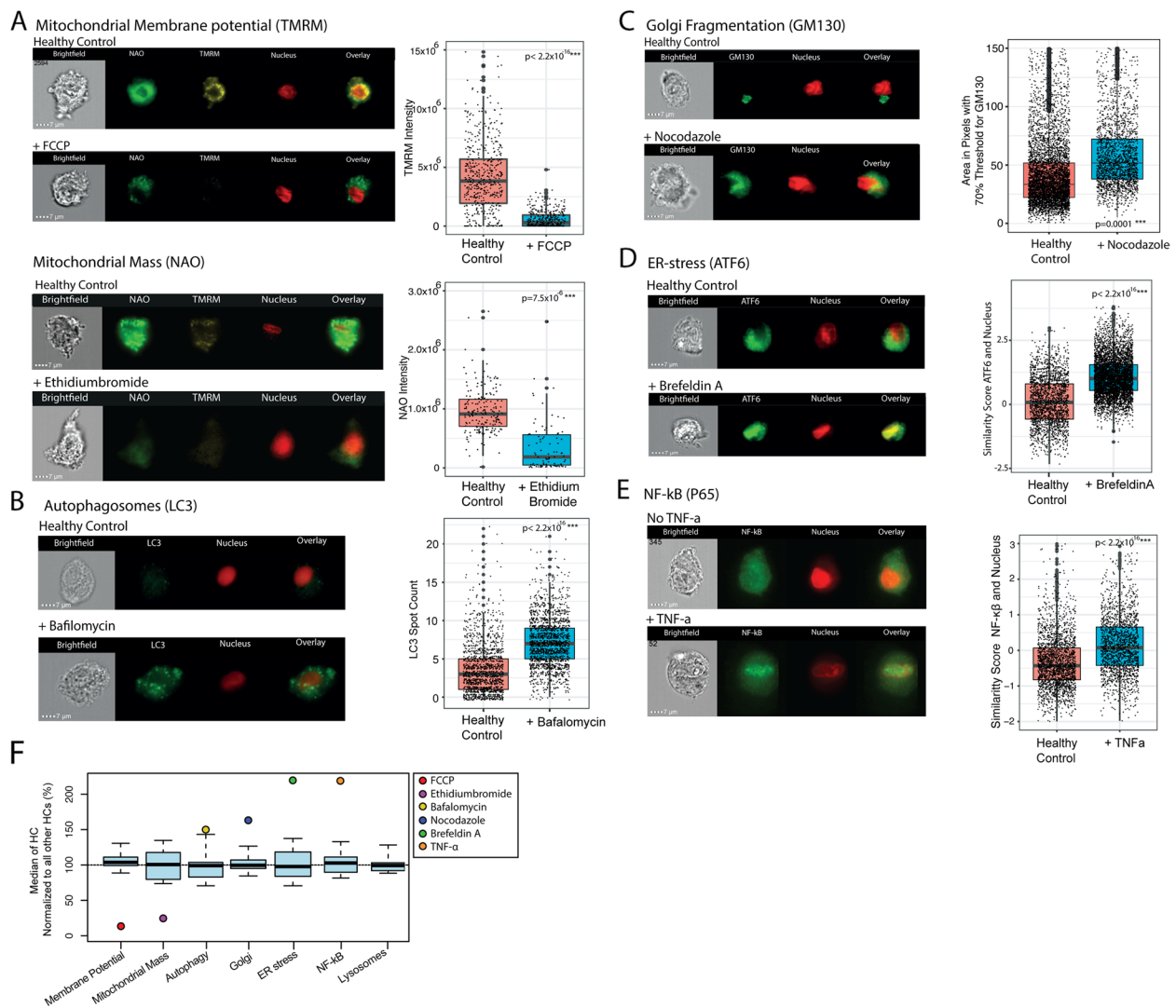


Fig. 1 Validation of assays using molecular compounds. **A** Representative IFC images of the mitochondrial staining (NAO and TMRM). The top two images show NAO/TMRM staining before and after FCCP treatment. The boxplot shows the intensity in pixels of the TMRM staining within the Object mask, which was used to quantify membrane potential. The bottom two images show the NAO/TMRM staining before and after ethidium bromide treatment. The boxplot shows the intensity in pixels of the NAO staining for both conditions, which was used to quantify mitochondrial mass. **B** Representative IFC images of the autophagy staining (LC3). When autophagy is induced with bafilomycin, the autophagosomes become visible. The boxplot shows the number of autophagosomes per cell (Spot Count) using the Spot mask (Bright, 10, 0, 2). **C** Representative IFC images of a cell with a healthy and intact Golgi and a cell with fragmented Golgi after the addition of nocodazole. The boxplot shows the area of the Golgi staining after applying a 70% intensity threshold. During nocodazole treatment, the surface area of the Golgi system becomes larger, indicating that the Golgi system is fragmented. To quantify fragmentation, both surface area as well as minor axis intensity were used (Additional File 1: Figure S3). **D** Representative IFC images of the ATF6 staining. When ER stress is triggered, ATF6 translocates to the nucleus. The boxplot shows the similarity score between the nuclear staining and the ATF6 staining, which was used as a measure to quantify ER stress. **E** Representative IFC images of the NF-κB staining (p65). Upon NF-κB activation, p65 translocates to the nucleus. The boxplot shows the similarity between the nuclear staining and the p65 staining, which was used as a measure to quantify NF-κB translocation. All boxplots represent one single experiment, and one treated and one untreated condition. The length and concentration of drug treatment are described in the "Methods" section. The boxplot upper and lower hinge reflect the 25 and 75% percentiles and the black line reflects the median. The upper and lower whisker extend to 1.5 * IQR. Data beyond the end of the whiskers are plotted as large black circles. All statistics were calculated using nonlinear mixed effect models. $p < 0.05^*$, $p < 0.01^{**}$, $p < 0.001^{***}$, $p < 0.0001^{****}$. **F** Boxplots showing the natural variation of assays in healthy controls and the percentage values of the healthy controls treated with the molecular compounds from Fig. 1A–E. For the healthy control range, the median value of the designated feature for each assay was compared to the mean all other healthy controls taken along in the same run and converted to percentages. For the compounds, the median value of the feature for the compound-treated healthy control was divided by the median value for the untreated control and converted to percentages. The compound treated-control values are indicated as colored dots. The boxplot upper and lower hinge reflect the 25 and 75% percentiles and the black line reflects the median. The upper and lower whisker extend to 1.5 * IQR

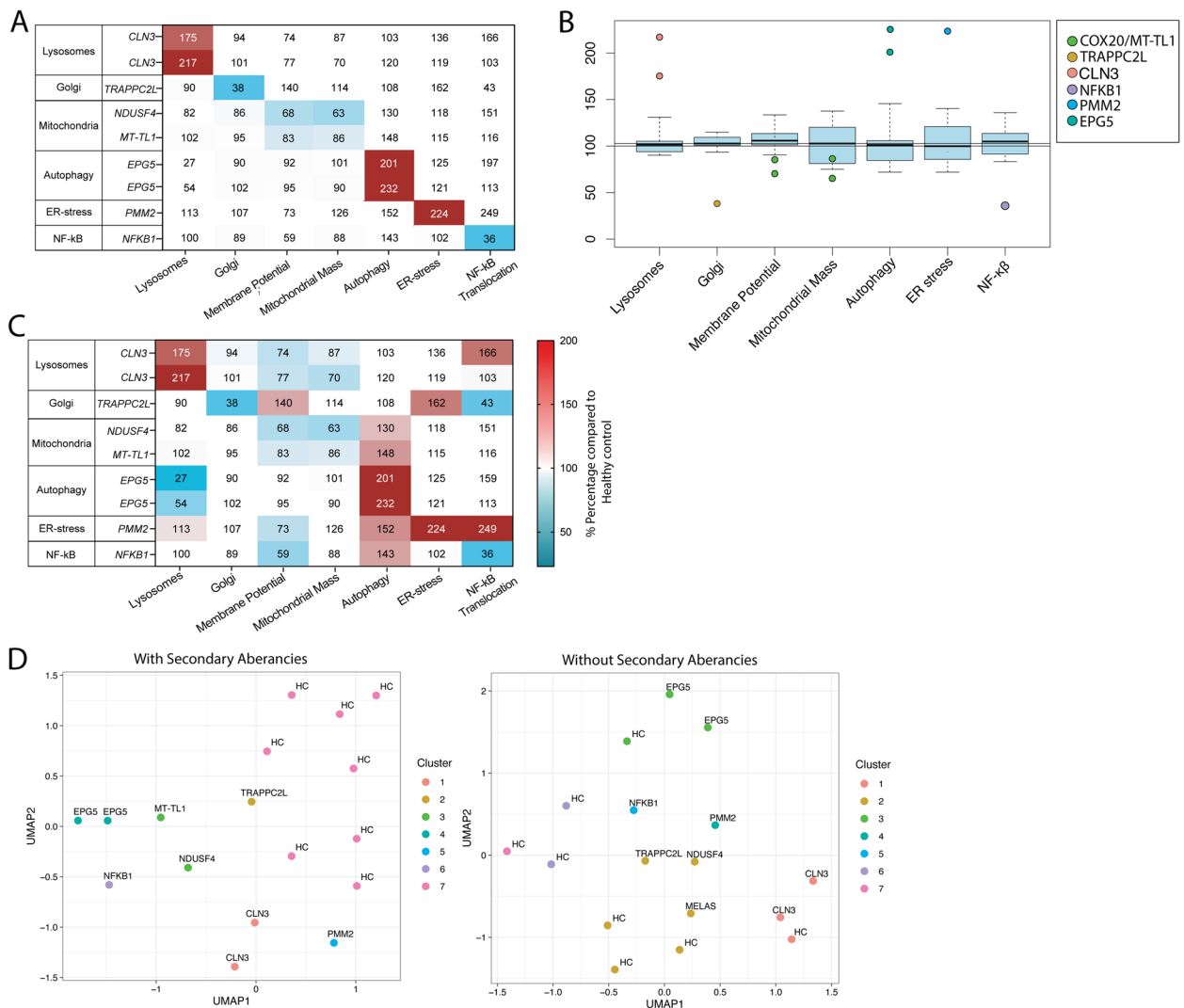


Fig. 2 Validation of assays in positive control patients. **A** Heatmap showing the values for each assay for the positive control patients compared to healthy controls ($N=3$) taken along in the same experiment. Each experiment was performed once. The primary abnormalities (expected deviations from normal values in the main phenotype of interest) for the positive control patients are colored using a color gradient (0–200%). **B** Showing the same graph as in Fig. 1F, where the healthy control reference range for all six assays is indicated in blue. The red dots refer to the positive control values and reflect the same values as observed in **A**. **C** Showing a similar heatmap as in **A**, but here all features are color-coded, based on the degree of abnormality outside of the healthy control range to the same scale as in Fig. 2A. **D** UMAP plots (Manhattan distance, neighbors=8, minimal distance=0.01) showing the clustering performance when combining all six assays (left), or when only the primary assay aberrancies were used (right). Clustering was performed using Manhattan Distance followed by average linkage clustering. Input for the plots were the percentage values as shown in Fig. 2C. For the UMAP plot and clustering based on the primary aberrancies only, secondary aberrancies were set to 100%

UMAP with specific parameters, setting the number of neighbors to 8 and the minimum distance to 0.01, which were determined through exploratory analysis. To create Fig. 4, raw feature values were extracted as.txt files. The mean value for each patient for each feature was divided by the mean value of all three healthy controls analyzed within the same experiment. The healthy control feature values were divided by the means of all other healthy

controls analyzed within the same experiment. Columns containing significantly large foldchange values (<0.15 or >6) were removed. This data can be found at <https://doi.org/10.6084/m9.figshare.28082345.v1>. [27].

Before UMAP and clustering, the entire data frame was scaled and centered. For clustering analyses using 1800 features, similarity was calculated using Euclidean distance, and clustering was performed using Ward’s method. We configured UMAP with specific

parameters, setting the number of neighbors to 4 and the minimum distance to 0.01, which were determined through exploratory analysis.

“Cluster characteristics” were determined by extracting features with a foldchange < 0.5 and > 1.5 in individuals included in the cluster. Highly correlating features were removed from the graph (Pearson correlation coefficient > 0.9) to enhance graph readability.

Functional assays for individuals with VUS in well-known disease genes

To validate the specificity of the IFC assays for individuals with *CLN3* VUS, *TAZ* VUS, *DLPI* VUS, *ACAD9* VUS, and *EPG5* VUS, diagnostic assays were used. To assess pathogenicity of *CLN3* variants, lymphocytes with vacuoles and the number of vacuoles per lymphocytes were assessed as described previously. Data was acquired using FACSCanto II and analyzed using FACS Diva Version 6.13 (BD Biosciences) or FlowJo version 7.6.5 software [28].

Quantification of MLCL/CL levels in individuals with *TAZ* variants was performed in dried blood spots using UHPLC-mass spectrometry [29].

For individuals with *DLPI* variants, peroxisomes were examined with the use of immunofluorescence microscopy with antiserum against peroxisomal catalase [30]. To examine mitochondria, fibroblasts were cultured on coverslips, incubated for 30 min with 50 nM of MitoTracker Green FM dye (Molecular Probes) and examined with the use of fluorescence microscopy at 488 nm [31]. Autophagy defects were assessed in individuals with *EPG5* variants using western blot probed against LC3-I, LC3-II, and p62 [32].

Data analysis and statistics

To calculate statistics in Fig. 1, nonlinear mixed effect models were used. Statistical analyses were performed

using Prism (Version 9.3.0, GraphPad Software). Statistics were only calculated if the number of patients exceeded three. If not shown, statistics were not assessed. R and R-studio were used to calculate statistics [33]. The following R packages were used for analysis: umap (0.2.10.0) [34], dplyr (1.1.3) [35], ggplot2 (3.4.3) [36], ggfortify (0.4.16) [37], ggforce (0.4.1) [38], cluster (2.1.4) [39, 40], factoextra (1.0.7) [40], miscTools (0.6–28) [41], caret (6.0–94) [42].

Results

Assay selection

For this study, we included six essential cellular pathways that could be morphologically assessed, and for which a reliable marker was available. Selection criteria can be found in Additional File 1: Table S1. Out of 10 pathways eligible for inclusion in this study, we included six assays that quantified morphology and function of mitochondria, autophagosomes, lysosomes, Golgi, ER stress, and NF- κ B translocation (Table 1). All assays were set up in primary dermal fibroblasts since these could easily be obtained from patients and their large cytoplasm allowed proper visualization of organelles.

Assay and feature validation

After optimizing antibody concentrations and assay conditions, we set out to evaluate whether the six assays were able to detect significant cellular changes in the selected pathways. As positive controls, we used a set of molecular compounds known to affect the specific pathways (Fig. 1A–F, Table 1). For quantification, we used features and masks derived from literature [50, 52, 54, 56–58]. For the LAMP1 assay, a novel feature and mask were designed based on the two positive control patient fibroblasts. For each assay and feature, we found significant differences between healthy control fibroblasts with and without molecular compounds (Fig. 1A–F, Additional

(See figure on next page.)

Fig. 3 Imaging flow cytometry (IFC) results of individuals with VUS in well-known disease genes. **A** UMAP plot (Manhattan distance, neighbors = 8, minimal distance = 0.01) showing the healthy controls (HC), individuals with VUS(es), and positive control counterparts matching the individuals with VUS in well-known disease genes. Normalized percentage values as shown in Table 2 were first scaled and used as input for UMAP. Most individuals with VUS clustered together with their positive control counterparts on UMAP, suggesting similar underlying mechanisms of disease. Only the individual with *EPG5* VUS clustered with healthy controls. **B** Bar graph showing aberrancies for two patients with pathogenic variants in *CLN3* and individuals with *CLN3* VUSes (CLN3 VUS). **C** Bar graph showing the Z-scores of the individual with *ACAD9* VUS and its positive control counterpart (one patient with pathogenic *ACAD9* variants) for Golgi, NF- κ B, and mitochondrial assays. **D** Bar graph showing aberrancies for one patient with a pathogenic variant in *TAZ* and one individual with *TAZ* VUS (TAZ VUS) for Golgi and mitochondrial assays. **E** Bar graph showing the Z-scores of the individuals with *DLPI* VUS and their positive control counterpart (one patient with a pathogenic *DLPI* variant) for the NF- κ B and the mitochondrial assay. **F** Bar graph showing the Z-scores for the individual with *EPG5* VUS and two patients harboring pathogenic *EPG5* variants for the autophagy assay (LC3—Spot Count) and LAMP1 assay (LAMP1—Internalization). For all bar charts, the raw values for each experiment were converted to Z-scores. The mean of all single cell Z-scores was calculated for each individual. The bars represent the mean and the error bars represent the range for healthy controls, individuals with VUS or patients with pathogenic variants. Each dot represents the mean Z-score per donor. Each experiment was performed once, and at least three healthy controls were included for each experiment, except for the mitochondrial experiment, where only one healthy control was included

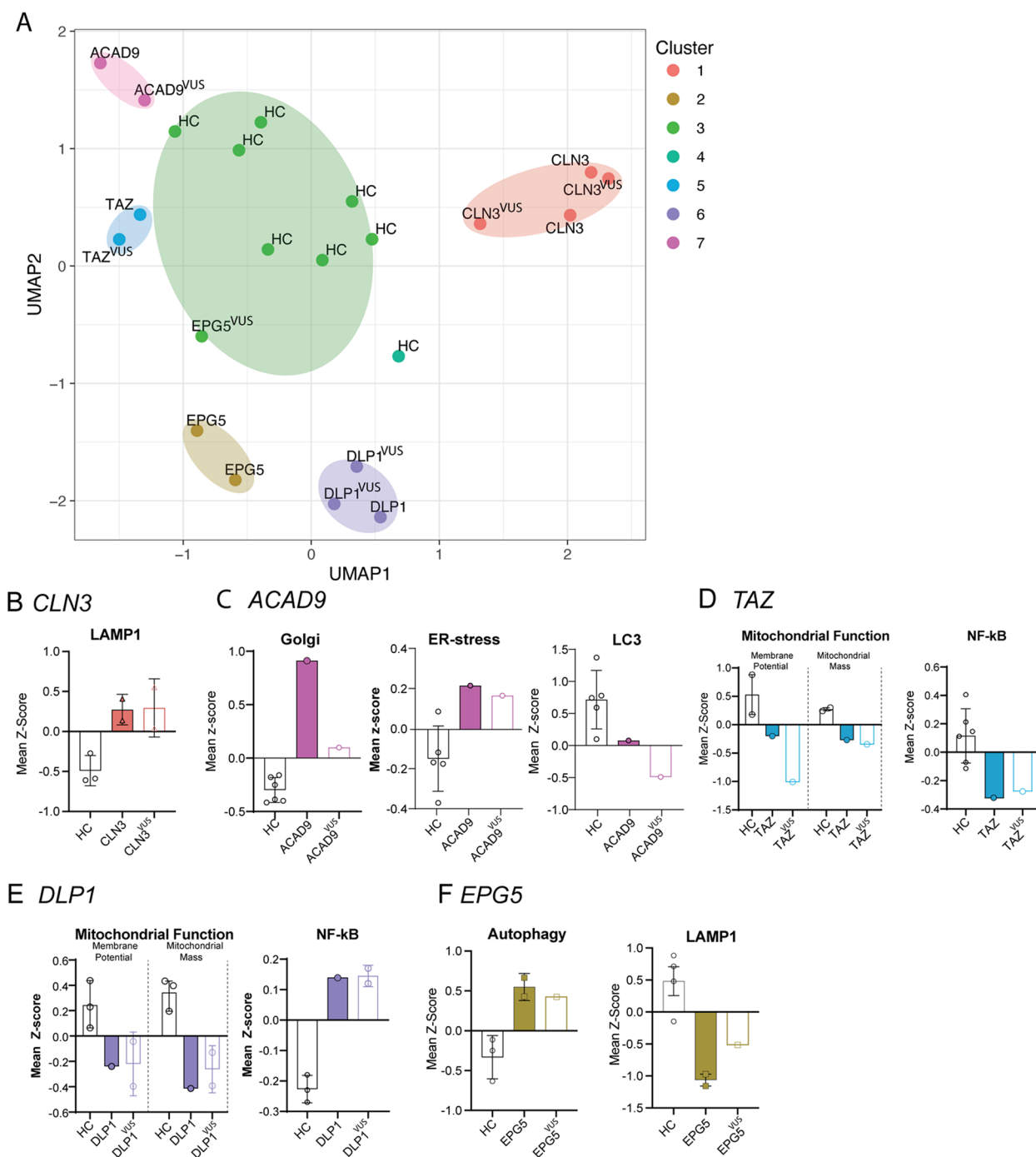


Fig. 3 (See legend on previous page.)

File 1: Table S2), indicating specificity of assays and features. In the absence of a molecular compound known to induce lysosomal accumulation, validation of the LAMP1 assay was based on two positive control patients alone.

Establishing a healthy reference range and assessing the effect of passage number and confluence on IFC assays
 To assess interindividual variation and to set reference values as a benchmark, we included eight healthy control fibroblast lines (Fig. 1F, Fig. 2B). We observed that certain

assays, including ER-stress, NF- κ B translocation, and mitochondrial mass, exhibited high variability among healthy controls. We hypothesized that some cellular phenotypes, like Golgi morphology and lysosomal size, are more tightly regulated since larger fluctuations could trigger cell death. In contrast, features such as ER stress and NF- κ B translocation may show greater variability due to shifts in activation thresholds, which can be influenced by previous cellular stressors [59–61]. For all assays, we found that variation in confluence—when kept within the advised confluence range (30–80%)—did not significantly affect assay results ($p > 0.05$) (Additional File 1: Figure S2). Passage number differences larger than five passages between donors were found to significantly affect Golgi fragmentation and mitochondrial function (Additional File 1: Figure S3) (IQR < 25% or IQR > 75%). Therefore, for these two assays, we kept patient fibroblasts and healthy control fibroblasts at similar passage numbers (< 5).

Cellular phenotypes are consistent among positive controls

Next, we verified assay sensitivity through the inclusion of positive control patients. These individuals were chosen based on literature indicating that their respective diseases could trigger discernible alterations in one of the six assays (Table 1). We found all positive patient controls showed significant changes on the assays for which

they were selected, indicating assay sensitivity (Fig. 2A, Fig. 2B, Additional File 1: Table S2). Additionally, the similar changes observed in two siblings with pathogenic *CLN3* variants, both showing enlargement of the lysosomal compartment, and in fibroblasts derived from siblings with pathogenic *EPG5* variants, showing increased autophagy, indicates that assays are consistent among patients with the same disorder (Fig. 2A).

We suspected that aberrancies in positive patient controls extended beyond the cellular pathway for which they were primarily selected. For example, it is well-known that mitochondrial disease patients exhibit increased autophagy due to a pseudo-starvation response [62]. Indeed, we found that mitochondrial disease patients showed increased autophagy (Fig. 2C). Moreover, patients with pathogenic variants in *EPG5* showed decreased numbers of lysosomes (Fig. 2C), corresponding with the pathophysiological mechanisms of pathogenic *EPG5* variants that show impaired autophagosome-lysosome transition [49]. Additionally, we found that patients with *EPG5* and *CLN3* pathogenic variants both showed increased ER stress (Fig. 2C). Putatively, autophagic and lysosomal protein degradation is impaired in these patients, triggering ER stress [63].

Based on these results, we suspected that the combination of primary and secondary aberrancies would lead to more specific disease profiles. To evaluate the

(See figure on next page.)

Fig. 4 Imaging flow cytometry results for individuals with VUS in GUS. **A** UMAP showing clustering based on six assays for healthy controls (HC), positive control patients, and 13 individuals with VUS in GUS. Normalized percentage values as shown in Table 3 were scaled and used as input for UMAP. **B** Bar graph showing the Z-scores of individuals 106 and 211 and patient with pathogenic *ERCC1* variants, for the Golgi, LAMP1, and mitochondrial assay. For the bar charts, the raw values for each experiment were converted to Z-scores. The mean of all single cell Z-scores was calculated for each individual. The bars represent the mean and the error bars represent the range for healthy controls, individuals with VUS or patients with pathogenic variants. Each dot represents the mean Z-score per donor. Each experiment was performed once, and at least three healthy controls were included for each experiment, except for the mitochondrial experiment, where only one healthy control was included. **C** UMAP of the healthy controls (HC), positive control patients, and the individuals with VUS in GUS. To create the plot, all 1800 features were used, including those quantifying nuclear and brightfield intensity and morphology. Each patient was normalized against three healthy controls taken along in the same experiment. The circles were drawn using the ggforce package. **D** Showing the cluster characteristics of the cluster with the individuals with *LIMK1* genetic variants (093 and 140). The dot plot on the left shows the features with foldchange < 0.5 and > 1.5 in both individuals compared to healthy controls. The median foldchange values for the two individuals is shown. Highly correlating features were removed from the graph (Pearson correlation coefficient > 0.9) to enhance graph readability. The increased nuclear intensity observed in both individuals with *LIMK1* genetic variants suggests increased numbers of cells in S/M phase. The histogram plot shows the distribution of nuclear intensity for single cells. For this plot, healthy controls ($N = 3$) were merged, and individuals with *LIMK1* VUS were merged ($N = 2$). The purple square indicates the gating that was used to determine the percentage of cells that were in the S/M phase. The bar chart shows the percentage of cells in S/M phase for each patient. Each dot represents the percentage of cell in S/M phase per donor. On the right, two representative examples of the autophagy staining are shown. For the images, the intensity threshold was set at 50%. **E** Showing the cluster characteristics of the cluster of the patient with pathogenic *ERCC1* variants and individuals 106, 211, and 216. The dot plot on the left shows the features with foldchange < 0.5 and > 1.5 in both individuals compared to healthy controls. The median foldchange values for the individuals is shown. Features with Pearson correlation coefficient > 0.9 were removed to enhance graph readability. The histogram plot shows the distribution of the Contrast feature for healthy controls ($N = 3$) and individuals 106, 211, and 216. On the right, representative examples of IFC images of healthy control fibroblasts and individual 106 and 211 are shown. The histogram plot on the far right shows the distribution of the H Energy Std_5 of the autophagy staining for healthy controls ($N = 3$) and individuals 106 and 211. On the right, representative examples of IFC images of healthy control fibroblasts and individuals 106 and 211 are shown

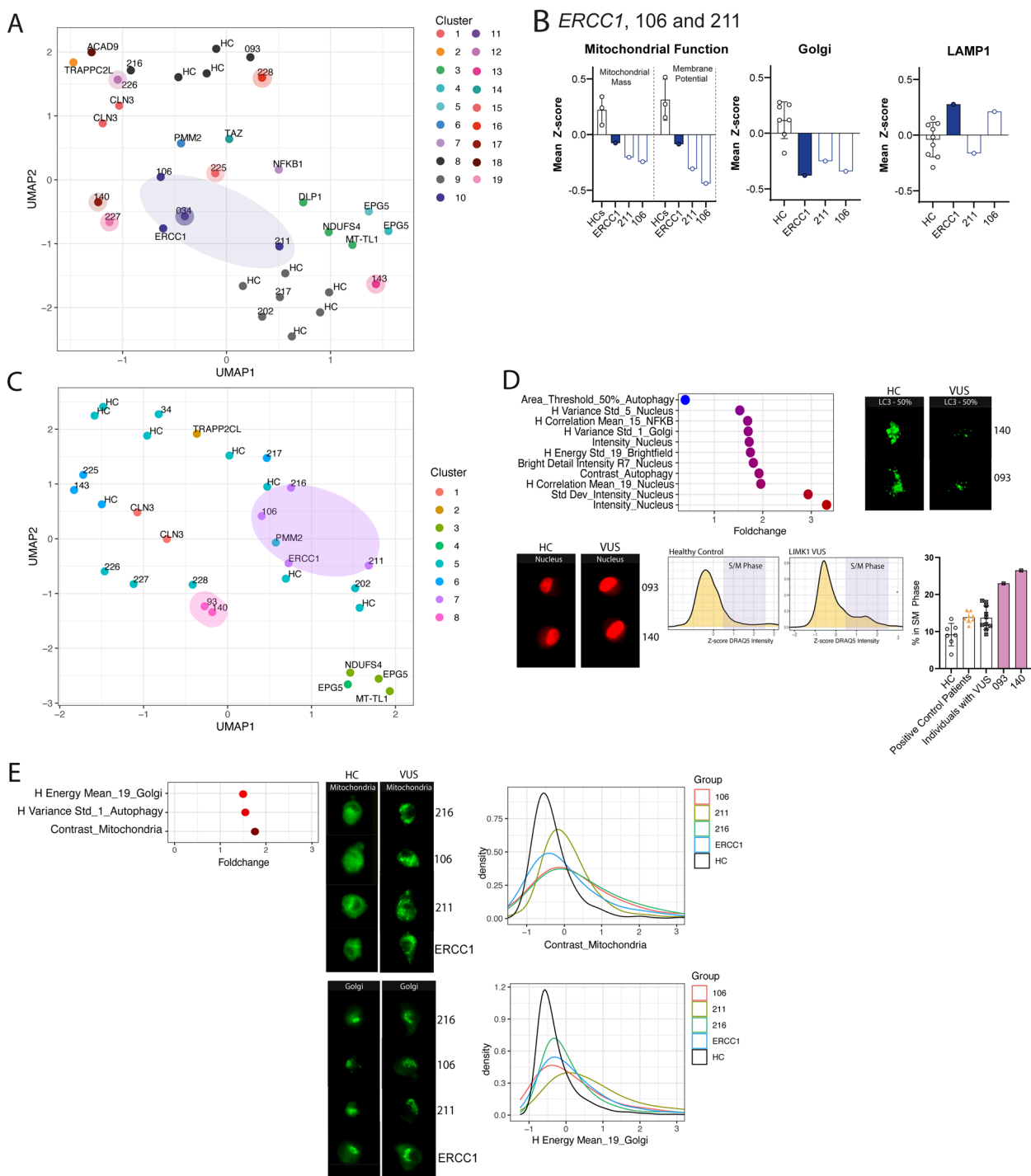


Fig. 4 (See legend on previous page.)

added benefit of using multiple assays, we assessed the performance of clustering algorithms when it comes to separating diseases from each other and from healthy controls. Indeed, we found that combining the six assays yielded specific clusters that corresponded with

the specific diseases in the positive patient control cohort (Fig. 2D, Additional File 1: Table S3). In contrast, clustering based on primary assay results alone did not allow separation of positive controls from healthy controls. Additionally, it mistakenly clustered the patient

Table 1 Overview of the six IFC assays quantifying six different aspects of cellular health. All assays were validated using compounds known to cause specific changes in the targeted pathway, serving as positive controls. Next, all assays were validated using patient cells, with diseases known to cause specific changes in the pathway of interest (positive patient control)

Primary assay	Marker	Molecular compound	Positive patient control
Mitochondrial mass	NAO	Valproic acid [43]	Polymerase- γ (<i>POLG</i>) pathogenic variants [44]
Membrane potential	TMRM	FCCP [45]	Mitochondrial disease patients with <i>mt-TL1</i> or <i>NDUSF4</i> pathogenic variants [46, 47]
Autophagy	LC-3	Bafilomycin and starvation [48]	<i>EPG5</i> pathogenic variants [49]
Lysosomal accumulation	LAMP-1	NA	<i>CLN3</i> pathogenic variants [28]
ER stress	ATF6	Brefeldin A [50]	<i>PMM2</i> pathogenic variants [51]
Golgi fragmentation	GM130	Nocodazole [52]	<i>TRAPPC2L</i> pathogenic variants [53]
NF- κ B translocation	p65	TNF- α [54]	<i>NFKB1</i> pathogenic variants [55]

Table 2 Showing the IFC assays results in individuals with VUS in known disease genes and positive control patients. The population means in individuals were compared to healthy controls and shown here as percentages. In bold, the percentages that fell outside of the healthy control reference range are shown

Patient ID	Gene	Golgi	ER stress	Autophagy	Lysosomes	Membrane potential	Mitochondrial mass	NF κ B-translocation
33	<i>CLN3</i>	94%	136%	103%	175%	74%	87%	166%
34	<i>CLN3</i>	101%	119%	120%	217%	77%	70%	103%
31	<i>CLN3</i> ^{VUS}	106%	147%	111%	213%	84%	88%	234%
35	<i>CLN3</i> ^{VUS}	103%	108%	87%	167%	127%	122%	106%
07	<i>EPG5</i>	90%	125%	201%	27%	92%	101%	159%
08	<i>EPG5</i>	102%	121%	232%	54%	95%	90%	113%
250	<i>EPG5</i> ^{VUS}	97%	135%	152%	83%	85%	89%	98%
252	<i>DLP1</i>	99%	111%	99%	78%	79%	76%	140%
249	<i>DLP1</i> ^{VUS}	106%	114%	106%	97%	60%	62%	139%
253	<i>DLP1</i> ^{VUS}	89%	132%	94%	108%	90%	72%	146%
251	<i>TAZ</i>	116%	102%	116%	79%	87%	62%	58%
240	<i>TAZ</i> ^{VUS}	122%	160%	124%	112%	82%	67%	52%
261	<i>ACAD9</i>	51%	182%	77%	99%	103%	86%	65%
111	<i>ACAD9</i> ^{VUS}	39%	158%	46%	101%	116%	84%	57%

harboring *TRAPPC2L* pathogenic variants with mitochondrial disease patients.

IFC screening of individuals with VUS(es) in well-known disease genes

First, we assessed the potential of IFC assays for seven individuals with genetic variants classified as VUS(es) in well-known disease genes (VUS in gene) (Additional File 1: Table S2). For each fibroblast line of an individual with VUS (white rows in Table 2), fibroblasts of a patient with a pathogenic variant in the same gene (positive control counterpart) were included for comparison (green rows in Table 2).

When using all six assays, we found that 6/7 individuals showed highly similar IFC profiles and clustered together with their positive control counterpart (Fig. 3A). The two individuals with *CLN3* VUSes clustered towards

pathogenic *CLN3* variants, all of whom showed increased lysosomal size (Fig. 3B). The individual with *ACAD9* VUS and its positive control counterpart both showed increased Golgi fragmentation, increased ER stress and decreased autophagy, and clustered together (Fig. 3C). The individual with a VUS in *TAZ* clustered with the patient harboring a pathogenic variant in *TAZ*, based on mitochondrial dysfunction and decreased NF- κ B translocation (Fig. 3D). Two individuals with *DLP1* VUSes clustered with the patient with a pathogenic *DLP1* variant, based on mitochondrial dysfunction and increased NF- κ B translocation (Fig. 3E). *TAZ* and *DLP1* dysfunction were expected to predominantly result in mitochondrial dysfunction [31, 64]. While both cohorts indeed presented with mitochondrial dysfunction, differences in NF- κ B activation helped separate the individuals with *DLP1* variants from individuals with *TAZ* variants

(Fig. 3D/E). The individual with *EPG5* VUS clustered with healthy controls instead of pathogenic *EPG5* variants, probably due to the mildly increased autophagy compared to patients with pathogenic *EPG5* variants (Fig. 3F).

Thus, IFC-based screening revealed highly specific phenotypic profiles for individuals with VUS that allowed clustering with their positive control counterpart, indicative of pathogenicity. Only the individual with *EPG5* VUS showed similar—but much milder—aberrancies and was clustered with healthy controls.

In order to verify the performance of IFC-assay based clustering, we validated whether the VUS(es) were truly pathogenic using well-established diagnostic assays. With the inclusion of these well-established functional results (PS3), all VUS(es) could be classified as pathogenic or likely pathogenic according to the ACMG guidelines, except for the *DLPI* and *EPG5* VUS, that remained classified as VUS (Additional File 1: Table S4). Individuals with *CLN3* VUS harboring a large 1-kb deletion in *CLN3* showed an increased number of vacuoles per lymphocyte and increased percentage of lymphocytes with vacuoles. Increased vacuolization in lymphocytes in a school-aged child with retinal dystrophy is pathognomic for Batten disease indicating pathogenicity (Additional File 1: Figure S4) [65–67]. The *TAZ* variant was classified as pathogenic due to its severely increased MLCL/CL ratio, which has high sensitivity and specificity to detect Barth Syndrome (Additional File 1: Figure S4) [29]. For the *ACAD9* VUS,

functional studies showed that the missense variant in this patient caused mildly decreased *ACAD9* activity (70% residual activity compared to WT-*ACAD9*) [68]. Individuals 249 and 253, both harboring heterozygous missense *DLPI* variants, showed mild mitochondrial fission and peroxisomal aberrancies upon microscopy, characteristic of either MFF or *DLP1* dysfunction [69–72]. Individual 253 lacked the peroxisomal aberrancies typically seen, suggesting that the variants in this patients might have a milder impact on overall protein function. Concurrently, IFC-screening revealed milder aberrancies for individual 253. The *DLPI* variant of individual 249 was considered likely pathogenic based on ACMG guidelines (Additional File 1: Table S4). Due to the absence of typical peroxisomal aberrancies in individual 253, this *DLPI* variant remained classified as VUS (Additional File 1: Table S4).

Individual 250 harbored a homozygous missense *EPG5* variant. Western blot probed against p62/LC3 revealed only mildly increased autophagy for this individual (data not shown). Based on these results and ACMG guidelines, the variant was classified as VUS (Additional File 1: Table S4).

Thus, IFC assays correctly clustered individuals with *CLN3*, *TAZ*, *DLPI*, and *ACAD9* VUS with their positive control counterparts, based on diagnostic assay results and ACMG guidelines. The uncertain pathogenicity of the *EPG5* variants was reflected in IFC assays, indicating the variant might result in a very mild cellular phenotype or is not pathogenic.

Table 3 Showing the individuals without VUS in well-known disease genes. The population means in these individuals were compared to healthy controls and shown as percentages. For each of the six assays, the features as shown in Table 1 were used for quantification. Percentage values highlighted in bold indicate the values are outside the reference range measured in healthy controls

Patient ID	Gene	Golgi	ER stress	Autophagy	Lysosomes	Membrane potential	Mitochondrial mass	NFκβ-translocation
143	<i>CSDE1</i> ^{VUS}	32%	72%	112%	62%	47%	79%	149%
140	<i>LIMK1</i> ^{VUS}	112%	173%	90%	153%	138%	66%	160%
093	<i>LIMK1</i> ^{VUS}	98%	145%	95%	158%	98%	119%	111%
225	<i>ZNF806</i> ^{VUS}	63%	186%	81%	135%	68%	48%	167%
227	<i>PDE3B</i> ^{VUS}	112%	141%	154%	130%	119%	95%	167%
228	<i>MMS19</i> ^{VUS}	112%	142%	99%	106%	96%	146%	201%
034	NA	99%	113%	126%	146%	63%	153%	183%
211	<i>DLGAP2</i> ^{VUS} , <i>TNKS</i> ^{VUS} , <i>BLM</i> ^{VUS}	118%	107%	88%	75%	73%	48%	109%
106	<i>RAD54L2</i> ^{VUS}	105%	111%	90%	106%	81%	77%	69%
226	<i>PDE4DIP</i> ^{VUS}	90%	33%	124%	152%	127%	97%	66%
216	NA	114%	152%	111%	104%	124%	99%	79%
202	<i>MEIOX</i> ^{VUS}	132%	78%	95%	81%	101%	101%	97%
217	<i>EIF4ENIF1</i> ^{VUS}	109%	82%	106%	68%	100%	66%	111%

IFC assays for individuals without VUSes in well-known disease genes

Next, we assessed the potential of our platform for individuals that did not harbor VUSes in well-known disease genes. Many of these genes had not been linked to monogenic diseases, and their functions were sometimes unknown. These genes are referred to as genes of uncertain significance (GUS) (Additional File 1: Table S5). We found all individuals in this group showed aberrancies on at least one of the six assays (Table 3). To allow better understanding of the IFC aberrancies found, we assessed whether fibroblasts of these individuals behaved analogously to any of the positive control patient fibroblasts used in this study. As expected, we did not identify relevant cluster formation (Fig. 4A). However, we did find seven individuals with VUS showing a unique combination of IFC aberrancies, leading to them being clustered individually. In contrast, the remaining four individuals with VUS showed only very mild differences and clustered with healthy controls (Fig. 4A).

To increase the possibility of relevant cluster formation, we introduced a novel patient control with a DNA damage repair defect, assumed to have a similar phenotype as one of the individuals harboring a VUS in a gene associated with DNA damage repair (106, VUS in *RAD54L2*). [73] To this aim, we included fibroblasts of a patient with a pathogenic variant in *ERCC1*, c.693C>G [6]. We found that individual 106, but also individual 211, clustered with the patient with pathogenic *ERCC1* variants, based on decreased mitochondrial function and decreased Golgi fragmentation (Fig. 4B). These similarities suggest that the VUSes identified in individuals 106 and 211 might lead to defective DNA damage repair.

The six selected features may offer only a limited representation of all quantifiable changes that can occur in individuals with VUS. For example, alterations in the distribution, size, or shape of organelles may occur. Consequently, alongside a targeted analysis based on six assays, we employed an broadened, untargeted approach, that allowed quantification of many aspects of each of the six cellular pathways. To this aim, we extracted all built-in IDEAS features derived from all six assays (~300 features per assay, 1800 features in total), including those quantifying nuclear and brightfield images. To minimize batch effects, we normalized each individual to the healthy controls taken along in the same experiment (Additional File 1: Figure S5). Using all 1800 features, we identified three clusters of individuals with VUS that clustered away from healthy controls (Fig. 4C).

The first cluster consisted of two individuals (093 and 140) both harboring VUSes in *LIMK*. We found that their clustering was mostly the result of altered nuclear morphology and intensity (Fig. 4D). Most notably, nuclear

intensity (DRAQ5 intensity) was increased in these individuals, suggesting increased DNA content, and thus an increased number of dividing cells (S/M phase). After quantification of the number of cells in G1/S/M phase using DRAQ5 nuclear intensity (2N/4N peaks), we found that the individuals with *LIMK1* genetic variants had increased percentages of dividing cells (S/M phase) (Fig. 4D). Another characteristic of the cluster became visible when LC3 (autophagy staining) intensity threshold was set at 50%, revealing a lower total area of the autophagy staining.

The second cluster identified was similar as one of the clusters identified when using all six assays. Again, we found the cluster included the patient with pathogenic *ERCC1* variants and individuals 106 and 211. Additionally, individual 216 was added to this cluster (Fig. 4E). The cluster was characterized by enhanced contrast of the mitochondrial staining (NAO) and altered texture of autophagosomes and the Golgi system (Fig. 4E). Texture was quantified using Haralick (H) features [74], using different pixel sizes. Notably, one of the finer texture attributes (pixel size 1, H Variance Standard Deviation) showed significant alterations in the autophagy assay. Moreover, there were notable changes for the larger texture attributes of the Golgi assay (pixel size 19, H Energy Mean), corresponding to the observed disarray and irregular borders of the Golgi system, which were evident upon visual inspection (Fig. 4E). These irregular borders could have potentially affected the quantification of Golgi area and diameter, particularly following the application of a 70% threshold, which might explain the diminished Golgi fragmentation that characterized this cluster when looking at six features only.

To study whether the second cluster indeed correlated with DNA damage repair diseases, we performed follow-up experiments. For individual 106, that harbored a VUS in *RAD54L2* (NM_015106.2: c.389A>G, p.Gln130Arg), and clustered with the patient with pathogenic *ERCC1* variants, we assessed DNA damage repair capacity. We focused on DNA damage repair capacity after X-ray irradiation but also after etoposide treatment, a chemotherapeutic agent that stabilizes DNA topoisomerase II cleavage complexes (TOP2ccs), as *RAD54L2* is involved in TOP2cc resolution [73, 75]. As such, *RAD54L2* knockout cell lines show increased sensitivity to Etoposide treatment [73]. For comparison, we included patient fibroblasts of a patient with pathogenic *TDP2* variants, since *TDP2* is similarly involved in TOP2cc resolution and similarly shows increased sensitivity to etoposide [7]. While survival after X-ray irradiation was not appreciably affected, we observed decreased survival of fibroblasts from the individual with *RAD54L2* VUS upon etoposide treatment compared to

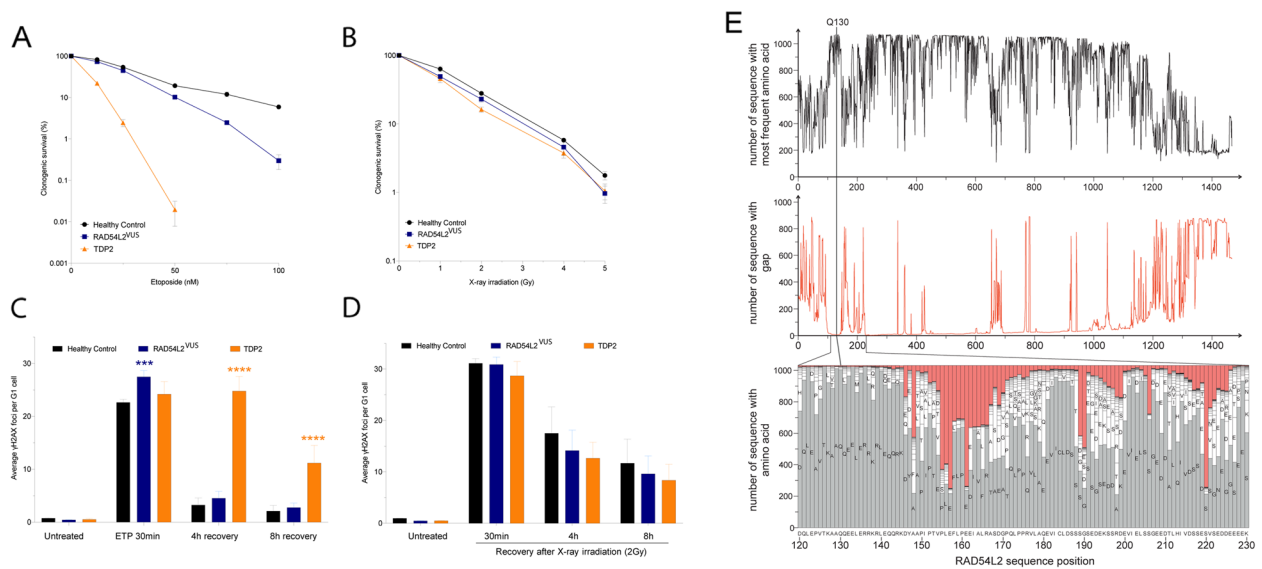


Fig. 5 Assessing pathogenicity of fibroblasts derived from individual 106 with *RAD54L2* VUS. **A,B** Clonogenic survival assay of patient fibroblasts upon treatment with the indicated doses of etoposide (**A**) or X-ray irradiation (**B**). **C** Number of γ H2AX foci in G1 cells (cyclin A negative) untreated or treated with 30 μ M etoposide (ETP) for 30 min, washed, and left to recover for 4 or 8 h. $n = 3$ independent experiments. Bars represent means \pm SEM. **D** Number of γ H2AX foci in G1 cells (cyclin A negative) untreated or irradiated with 2 Gy X-rays and left to recover for 30 min, 4 or 8 h. $n = 4$ independent experiments. Bars represent means \pm SEM. Statistics were calculated using 2-way ANOVA and Turkey's multiple comparisons test. **E** Showing conservation of *RAD54L2* amongst species. *RAD54L2* homologs were identified in about 1000 different species and pairwise aligned to the human sequence. As a measure for conservation, the number of sequences with the most frequently found amino acid (upper panel) and the number of sequences contacting a gap (middle panel) are determined per sequence position. The detailed frequencies are shown for the region containing Q130 (lower panel)

healthy control cells (Fig. 5A, B). In addition, compared to control cells, we observed increased γ H2AX foci in patient-derived fibroblasts of individual 106 immediately after etoposide treatment (0 h), which normalized after 4 and 8 h (Fig. 5C). Additionally, we did not observe any changes in γ H2AX foci levels in individual 106 upon treatment with ionizing radiations, in agreement to the survival data (Fig. 5D). To better interpret the pathogenicity of the *RAD54L2* variant, we studied *RAD54L2* and the specific region the variant was located in more in depth. *RAD54L2* has low tolerance against loss-of-function ($pLI = 1$) [76]. While structural information about the N-terminus of *RAD54L2* is lacking, we found that this region is highly conserved amongst 100 different species (Fig. 5E). The VUS is considered disease causing by MutationTaster [77] and has a CADD score of 25.6 (Additional File 1: Table S5). As such, we propose that the *RAD54L2* VUS could be considered likely pathogenic (ACMG: PS2, PM2, PP3). The inclusion of additional patients with *RAD54L2* variants could help reliably assess the genotype–phenotype correlation between *RAD54L2* and the clinical phenotype observed.

The third cluster we observed consisted of individuals 225, 143, 217, and one healthy control. The cluster was characterized by slightly decreased mitochondrial mass

values (data not shown). Due to the presence of a healthy control in the cluster, we decided not to study this cluster in depth.

In conclusion, we found that integrating all available IFC features ($N = 1800$) yielded two interesting clusters with distinct morphological aberrancies. In the individuals harboring *LIMK1* variants, we found increased mitosis and less bright autophagosomes. For individuals 211, 106, and 216, we found significant overlap with a patient harboring pathogenic *ERCC1* variants, characterized by altered Golgi- and mitochondrial morphology, which could be related to underlying DNA Damage Repair defects. Indeed, we found that one individual in this cluster harboring a VUS in *RAD54L2* showed decreased survival and increased γ H2AX foci after treatment with the chemotherapeutic agent etoposide, correlating with increased TOP2-mediated DNA damage [73].

Discussion

We present a novel imaging flow cytometry (IFC)-based platform to assess the clinical significance of variants of uncertain significance (VUS) by analyzing six key cellular processes. Significant assay sensitivity was confirmed with both compounds and positive controls, while combining these assays improved clustering. IFC

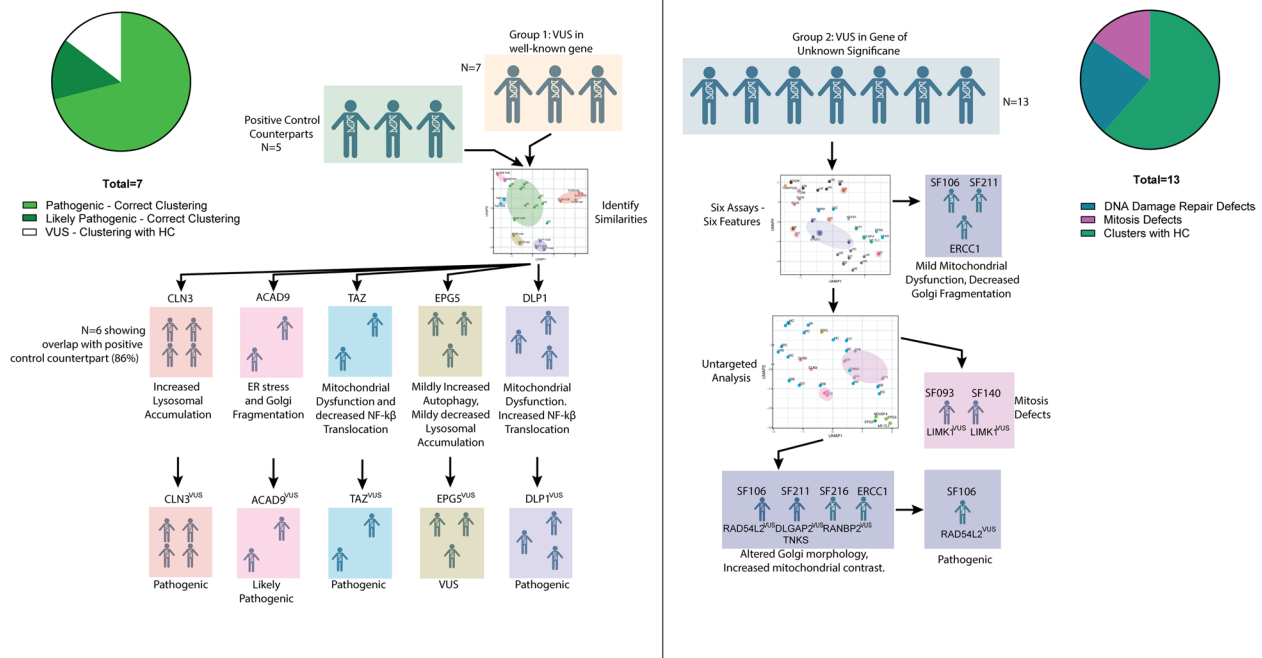


Fig. 6 Overview of imaging flow cytometry results for individuals with VUS. Left panel: The pie chart indicates the number on individuals with VUS in well-known disease genes that were correctly clustered with its pathogenic counterpart based on diagnostic assay results, leading to the VUSes being classified as pathogenic or probably pathogenic based on ACMG guidelines. Only one individual was clustered with healthy controls (HC). Diagnostic assays were inconclusive and the variant remained classified as VUS. The colored planes indicate the significant changes that were identified with IFC (upper row) and the ACMG classification of VUSes (lower row). Right panel: Pie chart indicating the clusters identified with IFC assays for individuals with VUS in genes of uncertain significance (GUS). Three individuals clustered with the patient with pathogenic *ERCC1* variants presumably based on altered DNA damage response, two individuals clustered together based on striking mitosis defects and the rest of the individuals clustered with healthy controls based on 1800 features. The colored planes indicate the significant changes found with IFC

identified similar phenotypic abnormalities in VUS cases within known disease genes, aligning with diagnostic expectations (Fig. 6). Additionally, in genes of uncertain significance, we observed significant changes across assays, allowing for the conceptualization of structured follow-up experiments. Two key clusters revealed specific mechanisms, such as mitosis and DNA repair defects (Fig. 6). Thus, IFC-based screening offers high-throughput cellular phenotyping to support VUS-related disease diagnosis.

We found IFC aberrancies for all 13 individuals with VUS in GUS, all of which could serve as a basis to structure subsequent experiments. However, the inclusion of a relevant positive control (DNA damage repair defect) to complement individuals with VUS in genes associated with DNA damage repair, provided a clearer picture of the potential pathophysiology at stake. Both the mitochondrial dysfunction and the altered Golgi morphology, that characterized the cluster, have been observed in patients with DNA damage repair defects, including *ERCC1* knockout models [78, 79]. Thus, the combination of mitochondrial dysfunction and altered Golgi morphology might be specific for DNA damage repair

defects. One of the individuals in the cluster, individual 106, harbored a de novo variant in *RADS4L2*, which interacts with *TOP2* to alleviate DNA damage [73, 75]. Functional assays showed that fibroblasts from this individual displayed increased γ H2AX foci and decreased survival after treatment with etoposide, suggesting that individual 106 indeed exhibits a DNA damage repair defect. Additionally, these results suggest that the VUS in *RADS4L2* could be causative of the patient's clinical phenotype. Another individual included in the cluster, individual 211, harbored multiple VUSes in the *DLGAP2*, *TNKS*, and *BLM* genes. Of those, *BLM* is a well-known disease gene, with bi-allelic variants leading to Bloom syndrome, a well-known DNA damage repair defect (OMIM #210,900). While the patient was solely a carrier of a pathogenic *BLM* variant, carriers of *BLM* variants can also exhibit mild DNA damage repair defects [80]. Potentially, this explains its clustering with other DNA damage related diseases. However, *TNKS* also has a role in DNA damage repair, and could have contributed to the phenotype as well [81]. Nonetheless, the similar cellular phenotypes observed in individuals 106, 211, and the patient with pathogenic *ERCC1* variants could

reflect similar functional cellular changes in response to impeded DNA damage repair, providing a relevant basis for further functional exploration. Additionally, these results indicate that the inclusion of relevant positive controls increases the diagnostic yield of IFC assays.

To broaden the scope of the IFC-based assays, we included all 1800 predefined IDEAS software-included features instead of just six. This untargeted approach led to the identification of two novel clusters. The first cluster consisted of two individuals harboring *LIMK1* variants, showing increased intensity of the nuclear (DNA) staining, suggesting that there was an increased number of cells in SM phase. Concurrently, *LIMK1* dysfunction has been associated with mitosis defects due to defective spindle positioning [82]. Therefore, the mitosis defects uncovered by IFC could indicate that the *LIMK1* variants identified in both individuals cause similar underlying pathophysiological defects. The second cluster identified when using the 1800 features was highly similar to the cluster found when using six features only, consisting of individuals 106, 211 and the patient with pathogenic *ERCC1* variants. Again, the cluster was characterized by altered Golgi and mitochondrial features, although the inclusion of 1800 features led to more precise quantification of these aberrancies, showing enhanced contrast of the mitochondrial staining and disorganized Golgi integrity. Additionally, expanding the scope to 1800 features led to the addition of individual 216 to the 'DNA damage cohort', although the absence of candidate VUSes in this individual limited the interpretation of its relevance. The lack of clustering among healthy controls when using all 1800 features might indicate the presence of noisy and irrelevant features within the dataset. With the addition of more healthy- and positive controls, computational models could be employed to prioritize meaningful features. Nonetheless, based on these results, we propose that studying all 1800 features has the potential of identifying more precise cellular phenotypes, which could be exploited to structure follow-up studies in a more targeted fashion.

So far, a limited number of studies have explored the potential of microscopy to determine the significance of VUS. Chao et al., [83] quantified the cellular location of PTEN in HeLa cells with different *PTEN* VUS to discern pathogenic variants from benign ones. Similarly, Ebrahim-Fakhari et al., [84] used microscopy to quantify ATG9A distribution, which helped to discern pathogenic *ATG9A* variants. While both studies seemed promising, their focus on a single gene limits a broader clinical applicability, since the heterogeneity of undiagnosed patient populations will require an untargeted approach. Fortunately, untargeted microscopic approaches have also been explored for VUS

elucidation, although not in pediatric patients. Caicedo et al., [85] found high accuracy when using microscopic screening to detect the pathogenicity of lung cancer variants using Cell Painting (RNA, ER, mitochondria, DNA and highly glycosylated proteins (AGPs) staining), while Ohya et al., [86] and Robhan et al., [5] found highly specific microscopic phenotypes after introducing various genetic deletions, that correlated with underlying pathophysiology. While these results are promising, high-throughput microscopy has not yet been used to study a large cohort of patients with VUS. A potential benefit of IFC over microscopy is the ability of newer IFC machines to perform cellular sorting after these assays. This makes IFC highly suitable for Multiplex Assay of Variant Effect (MAVE) studies, an approach that facilitates variant editing of single cells to study variant-induced cellular phenotypes in a high-throughput fashion [87–89]. Instead of focusing on the patients at hand, creating common variants in a large number of monogenetic disease genes and assessing those at a single cell level with IFC could help build a 'positive control atlas' for our assays, that can be used to cluster unknown variants.

For individuals with VUS in well-known disease genes, we found that IFC assays were able to detect relevant overlap with patients with pathogenic variants in the same gene, aiding the interpretation of underlying pathophysiology. The differentiating power of IFC for these individuals was enhanced by combining the six assays, since certain diseases appeared similar when looking at single axes only. For example, patients with pathogenic *DLP1* or *TAZ* variants primarily showed mitochondrial dysfunction, however, the increased versus decreased NF- κ B translocation made them cluster separately. These differentiating features are in line with previous work, showing decreased NF- κ B activation in tafazzin knockout iPSCs, putatively as a consequence of altered mitochondrial ROS signaling [90]. In contrast, HEK293 cells expressing mutant *DLP1* showed increased mitochondrial fusion and increased NF- κ B activity [91]. Thus, the integration of six assays provided enhanced discriminatory power, and revealed relevant underlying disease mechanisms for individuals with VUSes in well-known genes. To formally assess diagnostic accuracy of our IFC platform, additional patients need to be included as positive controls, to assess the inter-individual variability for the different assays. Additionally, the inclusion of patients with benign variants and patients with similar phenotypes could help determine the strength of our assays for determining pathogenicity. Lastly, it would be interesting to validate whether patients with milder phenotypes similarly display cellular phenotypes outside the healthy reference range. That being said, most genetic diseases are rare, and including sufficient

numbers to allow accurate pathogenicity prediction will remain challenging. Potentially, the use of single cell results rather than bulk medians will help to gather sufficient numbers to train classification models, although this will require optimization of batch effects, normalization, and noise filtering steps. Regardless, we expect a combination of in silico prediction tools, functional cellular models and the interpretation by expert clinicians will remain essential for the final judgement of pathogenicity prediction. Additionally, most endeavors to elucidate VUS nowadays exist of multiple experiments, where IFC-based assays could serve as the first step to structure these experiments. It will remain challenging to accurately quantify the value of having a valid starting point, despite its relevance in establishing diagnosis.

IFC has the potential to streamline multiple aspects of the diagnostic workflow. Firstly, in cases where individuals have variants of uncertain significance (VUS) in well-known genes lacking diagnostic assays, IFC-based assays could assist in interpreting pathogenicity. Establishing a public IFC database could ultimately eliminate the need for including patients with similar pathogenic variants as positive controls. Additionally, even in cases where diagnostic assays are available, IFC could offer an alternative requiring fewer assays and resources, while simultaneously aiding in the recognition of unknown disease entities by serving as a positive control. Secondly, for individuals with VUS in *GUS*, IFC based assays can lead to a more targeted diagnostic workflow by providing researchers with a sense of direction. For example, the striking mitosis defects found in individuals with *LIMK1* variants suggest that mitosis should be studied more in depth. Beyond its diagnostic applications, the high-throughput potential of IFC assays could be used to predict disease severity and therapeutic response. Previously, we found that LAMP1 accumulation assessed with IFC serves as a proxy for Batten disease severity [28]. The potential of the other IFC-based assays could be studied in a similar manner. Moreover, once a specific phenotypic profile for an individual with VUS is established and validated for diagnostic- and prognostic purposes, it can be used to screen for relevant therapies. The broadness of the screening would simultaneously allow for uncovering unexpected off-target effects. The IFC pipeline could be extended to include other relevant primary cell types derived from organs where the disease manifests. Our assays measure fundamental cellular processes that are likely involved in the pathophysiology of various cell types. In principle, any homogeneous cell type that can be suspended and fits within the 70-micron nozzle is suitable for these assays. A promising and patient-friendly approach for studying metabolic diseases involves using Neural Progenitor Cells derived from

nasal brush samples, offering a high-throughput method that captures disease-relevant tissue [92].

Here, we explored the potential of IFC-based cellular screening for individuals with a variety of VUSes in patient-derived fibroblasts. We provide evidence that IFC is able to delineate pathophysiological mechanisms in individuals with VUS(es) in well-known genes, based on similar cellular phenotypes compared to ‘true patients’, on assays of known relevance for underlying pathophysiology. Even in the most challenging group of individuals with VUS that underwent IFC-based screening, we found significant changes for all subjects and distinct disease signatures that offer novel insights into underlying pathophysiological mechanisms for 5 out of 13 patients. We anticipate that by broadening the spectrum of patients and diseases included in our study and implementing improved noise filtering steps and feature selection tools, the screening quality of IFC could be further enhanced. Given the versatility, simplicity, and high-throughput potential of our IFC-based screening platform, we believe its full capacity to elucidate pathophysiology and facilitate clinical applications in individuals with VUS and patients with genetic diseases is yet to be fully realized.

Conclusions

Here, we describe a novel imaging flow cytometry (IFC)-based screening platform, aimed to delineate the clinical significance of variants of uncertain significance (VUS) by providing insights into six pivotal cellular processes. We found that both compounds as well as positive control patients showed significant changes on cognate assays, indicating assay sensitivity, and combining the six assays enhanced clustering performance. For all individuals with VUS(es) in well-known disease genes, IFC-based screening identified similar aberrancies compared to corresponding positive controls, that aligned with diagnostic assay results, suggesting that IFC allows for accurate pathogenicity prediction. For individuals with VUS(es) in genes of uncertain significance, we found significant changes for each individual on one or more of six assays, which could be used to structure follow-up assays. Additionally, we found two relevant clusters that granted insights into highly specific pathophysiological mechanisms, for example by uncovering mitosis defects or DNA damage repair defects. Experimental follow-up of one of the individuals in this cluster revealed decreased survival and increased γ H2AX foci after chemotherapeutic treatment, indicative of a DNA damage repair defect. Based on these results, we propose that IFC-based functional screening allows for high-throughput characterization of cellular phenotypes, which can contribute to disease elucidation and subsequent diagnosis for individuals with VUS.

Abbreviations

VUS	Variant of uncertain significance
GUS	Gene of uncertain significance
IFC	Imaging flow cytometry
FCCP	Carbonyl cyanide-p-trifluoromethoxyphenylhydrazine
NAO	Nonyl Acridine Orange
TMRM	Tetramethylrhodamine, methyl ester
ETP	Etoposide
ACMG	American College of Medical Geneticist
MAF	Minor allele frequency
BSA	Bovine serum albumin
PBS	Phosphate buffered saline
TNF	Tumor necrosis factor
FBS	Fetal bovine serum
HBSS	Hank's Balanced Salt Solution
WSS	Within-Cluster-Sum of Squared Errors
UMAP	Uniform Manifold Approximation and Projection
MLCL/CL ratio	Monolysocardiolipin/cardioliipin ratio
MAVE	Multiplexed assays of variant effects

Supplementary Information

The online version contains supplementary material available at <https://doi.org/10.1186/s13073-025-01433-9>.

Additional file 1.

Acknowledgements

We thank Prof. Paul Coffey, Dr. Jorg Calis and Dr. Jorg van Loosdregt for their input during the project conceptualization. We would like to thank Dr. Arjan F. Theil and Prof. Dr. Wim Vermeulen for the relevant resources and advice on DNA Repair deficient disorders. Fibroblasts harboring ERCC1, TDP2 (850BR) pathogenic variants and control cells (1BR) were kindly provided by the Genome Damage and Stability Centre Research Tissue Bank (GDSC-RTB), University of Sussex.

Authors' contributions

Conceptualization: I.J.J.M., E.E.S.N., S.A.F., F.v.W., P.v.H.. Methodology: I.J.J.M., G.Z.V., G.D., S.J., E.E.S.N., S.A.F., F.v.W., P.v.H.. Formal Analysis: I.J.J.M., G.Z.V., G.D., P.v.H.. Investigation: I.J.J.M., H.R.W., G.D., G.Z.V., S.M., D.J.L., C.V., C.R., K.L.I.G., H.R., D.H.V.. Writing – Original Draft: I.J.J.M., E.E.S.N., S.A.F., F.v.W., P.v.H.. Writing – Review and Editing: I.J.J.M., H.R.W., G.D., G.Z.V., K.L.I.G., E.E.S.N., S.P., S.A.F., F.v.W., P.v.H.. Visualization: I.J.J.M., G.D., G.Z.V.. Supervision: E.E.S.N., S.P., S.A.F., F.v.W., P.v.H.. Funding Acquisition: I.J.J.M., S.A.F., P.v.H.. All authors read and approved the final manuscript.

Funding

This work was funded by the Wilhelmina Children's Hospital Stimulus Stipend 2019–2020 and the United For Metabolic Diseases Catalyst Grant 2023.

Data availability

IFC results derived from the six assays can be found in Table 2 and Table 3. The foldchange values for the untargeted analysis of 1800 features can be found at: <https://doi.org/https://doi.org/10.6084/m9.figshare.28082345.v128> The *RAD54L2* pathogenic variant has been deposited as SCV005387562 at Clinvar. [93].

Whole-exome sequencing (WES) data were obtained during clinical investigations for the patients included in this study. Due to patient confidentiality agreements, the WES data, including the clinical metadata and the exact location of the identified variants, cannot be made publicly available. Parental consent is available for sharing WES data if it directly adds to the diagnostic quest for the specific patient to whom the data pertain. We encourage interested researchers to contact the corresponding author to explore possibilities for data access in alignment with the above, which will be evaluated on a case-by-case basis and in compliance with institutional and ethical guidelines.

Declarations**Ethics approval and consent to participate**

All patients consented to use their residual material collected for diagnostic purposes in the Wilhelmina Children's Hospital metabolic biobank (TCBio 19–489/B and 22–284 (ImaVUS) <https://tcbio.umcutrecht.nl>). All procedures performed in studies involving human participants were in accordance with the ethical standards of the institutional and/or national research committee(s) and with the Helsinki Declaration (as revised in 2013).

Consent for publication

Only de-identified data was published in this work. All procedures performed in studies involving human participants were in accordance with the ethical standards of the institutional and/or national research committee(s) and with the Helsinki Declaration (as revised in 2013).

Competing interests

The authors declare that they have no competing interests.

Author details

¹Department of Metabolic Diseases, Division Pediatrics, Wilhelmina Children's Hospital University Medical Centre Utrecht, Utrecht University, Utrecht, the Netherlands. ²United For Metabolic Diseases (UMD), Amsterdam, the Netherlands. ³Department of Laboratory Medicine, Laboratory Genetic Metabolic Diseases, Amsterdam UMC - AMC, Amsterdam, the Netherlands. ⁴Cancer Research UK Cambridge Institute, University of Cambridge, Cambridge, UK. ⁵The Gurdon Institute and Department of Biochemistry, University of Cambridge, Cambridge, UK. ⁶Department of Biology, Concordia University, Montreal, QC, Canada. ⁷Department of Anatomy and Cell Biology, McGill University, Montreal, QC, Canada. ⁸Translational Metabolic Laboratory, Department of Neurology, Department of Human Genetics, Donders Institute for Brain, Cognition and Behavior, Radboud University Medical Center, Nijmegen, the Netherlands. ⁹The Hospital for Sick Children and Research Institute, The University of Toronto, Toronto, Canada. ¹⁰Department of Genetics, University Medical Center Utrecht, Utrecht, The Netherlands. ¹¹Department of Energy and Biotechnology, Flensburg University of Applied Sciences, Flensburg, Germany. ¹²Department of Pediatrics, Center for Lysosomal and Metabolic Diseases, Erasmus University Medical Center, Rotterdam, The Netherlands. ¹³Center for Rare Diseases, Erasmus University Medical Center, Rotterdam, the Netherlands. ¹⁴Center for Translational Immunology (CTI), University Medical Center Utrecht (UMC), Utrecht University (UU), Utrecht, The Netherlands.

Received: 3 May 2024 Accepted: 20 January 2025

Published online: 07 February 2025

References

- Richards S, Aziz N, Bale S, et al. Standards and guidelines for the interpretation of sequence variants: A joint consensus recommendation of the American College of Medical Genetics and Genomics and the Association for Molecular Pathology. *Genet Med*. 2015;17(5):405–24. <https://doi.org/10.1038/gim.2015.30>.
- Makhnoon S, Shirts BH, Bowen DJ. Patients' perspectives of variants of uncertain significance and strategies for uncertainty management. *J Genet Couns*. 2019;28(2):313–25. <https://doi.org/10.1002/jgc4.1075>.
- Gustafsdottir SM, Ljosa V, Sokolnicki KL, et al. Multiplex cytological profiling assay to measure diverse cellular states. *PLoS One*. 2013;8(12):e80999. <http://eutils.ncbi.nlm.nih.gov/entrez/eutils/elink.fcgi?dbfrom=pubmed&id=24312513&retmode=ref&cmd=prlinks>
- Chandrasekaran SN, Ceulemans H, Boyd JD, Carpenter AE. Image-based profiling for drug discovery: due for a machine-learning upgrade? *Nat Rev Drug Discov*. 2021;20(2):145–59. <https://doi.org/10.1038/s41573-020-00117-w>.
- Rohban MH, Singh S, Wu X, et al. Systematic morphological profiling of human gene and allele function via cell painting. *Elife*. 2017;6. <https://doi.org/10.7554/eLife.24060>
- Kashiyama K, Nakazawa Y, Pilz DT, et al. Malfunction of nuclease ERCC1-XPF results in diverse clinical manifestations and causes Cockayne

- syndrome, xeroderma pigmentosum, and Fanconi anemia. *Am J Hum Genet.* 2013;92(5):807–19. <https://doi.org/10.1016/j.ajhg.2013.04.007>.
7. Zagnoli-Vieira G, Bruni F, Thompson K, et al. Confirming TDP2 mutation in spinocerebellar ataxia autosomal recessive 23 (SCAR23). *Neurol Genet.* 2018;4(5). <https://doi.org/10.1212/nxg.0000000000000277>
 8. Karczewski KJ, Francioli LC, Tiao G. The mutational constraint spectrum quantified from variation in 141,456 humans. *Nature.* 2020;581(7809):434–43. <https://doi.org/10.1038/s41586-020-2308-7>.
 9. Donnelly P, Green ED, Knoppers BM, et al. A global reference for human genetic variation. *Nature.* 2015;526(7571):68–74. <https://doi.org/10.1038/nature15393>
 10. Zerbino DR, Achuthan P, Akanni W, et al. Ensembl 2018. *Nucleic Acids Res.* 2018;46(D1):D754–61. <https://doi.org/10.1093/nar/gkx1098>.
 11. Sherry ST, Kholodov MH, Ward M, et al. dbSNP: the NCBI database of genetic variation. *Nucleic Acids Res.* 2001;29(1):308–311. <https://academic.oup.com/nar/article-abstract/29/1/308/1116004>
 12. McKenna A, Hanna M, Banks E, et al. The Genome Analysis Toolkit: A MapReduce framework for analyzing next-generation DNA sequencing data. *Genome Res.* 2010;20(9):1297–303. <https://doi.org/10.1101/gr.107524.110>.
 13. Robert F Ernst, Mark van Roosmalen, Joep de Ligt, et al. UMCUGenetics/IAP: v2.7.0. Published online 2019. Accessed December 18, 2024. <https://zenodo.org/records/2565055#Xows-ogzY2w>.
 14. Tarasov A, Vilella AJ, Cuppen E, Nijman IJ, Prins P. Sambamba: fast processing of NGS alignment formats. *Bioinformatics.* 2015;31(12):2032–4. <https://doi.org/10.1093/bioinformatics/btv098>.
 15. Li H. Fast and accurate short read alignment with Burrows-Wheeler transform. *Bioinformatics.* 2009;25(14):1754–60. <https://doi.org/10.1093/bioinformatics/btp324>.
 16. Adzhubei IA, Schmidt S, Peshkin L, et al. A method and server for predicting damaging missense mutations. *Nat Methods.* 2010;7(4):248–9. <https://doi.org/10.1038/nmeth0410-248>.
 17. Kumar P, Henikoff S, Ng PC. Predicting the effects of coding non-synonymous variants on protein function using the SIFT algorithm. *Nat Protoc.* 2009;4(7):1073–81. <https://doi.org/10.1038/nprot.2009.86>.
 18. Grantham R. Amino acid difference formula to help explain protein evolution. *Science.* 1974;185(4154):862–4. <https://doi.org/10.1126/science.185.4154.862>.
 19. Pollard KS, Hubisz MJ, Rosenbloom KR, Siepel A. Detection of non-neutral substitution rates on mammalian phylogenies. *Genome Res.* 2010;20(1):110–21. <https://doi.org/10.1101/gr.097857.109>.
 20. Davydov E V, Goode DL, Sirota M, Cooper GM, Sidow A, Batzoglou S. Identifying a high fraction of the human genome to be under selective constraint using GERP++. *PLoS Comput Biol.* 2010;6(12). <https://doi.org/10.1371/journal.pcbi.1001025>
 21. Terhal PA, Vlaar JM, Middelkamp S, et al. Biallelic variants in POLR3GL cause endosteal hyperostosis and oligodontia. *Eur J Hum Genet.* 2020;28(1):31–9. <https://doi.org/10.1038/s41431-019-0427-0>.
 22. Monroe GR, Frederix GW, Savelberg SMC, et al. Effectiveness of whole-exome sequencing and costs of the traditional diagnostic trajectory in children with intellectual disability. *Genet Med.* 2016;18(9):949–56. <https://doi.org/10.1038/gim.2015.200>.
 23. Tang R, Prosser DO, Love DR. Evaluation of Bioinformatic Programmes for the Analysis of Variants within Splice Site Consensus Regions. *Adv Bioinformatics.* 2016;2016. <https://doi.org/10.1155/2016/5614058>
 24. Muffels Irena JJ, Rodenburg R, Willemsen HLD, et al. Imaging flow cytometry reveals divergent mitochondrial phenotypes in mitochondrial disease patients. *iScience.* 2025;28(1):111496. <https://doi.org/10.1016/j.isci.2024.111496>
 25. Diaz G, Diana A, Falchi AM, et al. Intra- and intercellular distribution of mitochondrial probes and changes after treatment with MDR modulators. *IUBMB Life.* 2001;51(2):121–6. <https://doi.org/10.1080/15216540152122139>.
 26. Bernardi P, Scorrano L, Colonna R, Petronilli V, Di Lisa F. Mitochondria and cell death. Mechanistic aspects and methodological issues. *Eur J Biochem.* 1999;264(3):687–701. <https://doi.org/10.1046/j.1432-1327.1999.00725.x>.
 27. Irena Josephina Johanna Muffels. Normalized data for all positive control patients, healthy controls and patients with VUS. FigShare. <https://doi.org/10.6084/m9.figshare.28082345.v1>
 28. Kuper WFE, Oostendorp M, van den Broek BTA, et al. Quantifying lymphocyte vacuolization serves as a measure of CLN3 disease severity. *JIMD Rep.* 2020;54(1):87–97. <https://doi.org/10.1002/jmd2.12128>.
 29. Vaz FM, van Lenthe H, Vervaart MAT, et al. An improved functional assay in blood spot to diagnose Barth syndrome using the monolysocardiolipin/cardiophilin ratio. *J Inher Metab Dis.* 2022;45(1):29–37. <https://doi.org/10.1002/jimd.12425>.
 30. Van Grunsven EG, Van Berkel E, Mooijer PAW, et al. Peroxisomal bifunctional protein deficiency revisited: Resolution of its true enzymatic and molecular basis. *Am J Hum Genet.* 1999;64(1):99–107. <https://doi.org/10.1086/302180>.
 31. Waterham HR, Koster J, van Roermund CWT, Mooyer PAW, Wanders RJA, Leonard JV. A Lethal Defect of Mitochondrial and Peroxisomal Fission. *N Engl J Med.* 2007;356(17):1736–41. <https://doi.org/10.1056/nejmoa064436>.
 32. Hori I, Otomo T, Nakashima M, et al. Defects in autophagosome-lysosome fusion underlie Vici syndrome, a neurodevelopmental disorder with multisystem involvement. *Sci Rep.* 2017;7(1). <https://doi.org/10.1038/s41598-017-02840-8>
 33. R Core Team. R: A language and environment for statistical computing. Published online 2021.
 34. McInnes L, Leland J, Healy J. UMAP: Uniform Manifold Approximation and Projection for dimension reduction. 2018. <https://doi.org/10.48550/arXiv.1802.03426>.
 35. Wickham H, François R, Henry L, Müller K, Vaughan D. dplyr: A Grammar of Data Manipulation. R package version 1.1.4. 2023. <https://github.com/tidyverse/dplyr>, <https://dplyr.tidyverse.org>.
 36. Wickham H. ggplot2. Springer New York; 2009. <https://doi.org/10.1007/978-0-387-98141-3>.
 37. Tang Y, Horikoshi M, Li W. ggfortify: unified interface to visualize statistical result of popular R packages. *The R Journal.* 2016;2(8):474–85. <https://doi.org/10.32614/RJ-2016-060>.
 38. Pedersen T. ggforce: Accelerating 'ggplot2'. R package version 0.5.0. 2024. <https://github.com/thomasps85/ggforce>.
 39. Maechler M, Rousseeuw P, Struyf A, Hubert M, Hornik K. cluster: Cluster Analysis: Basics and Extensions. R package version 2.1.8. 2023. <https://CRAN.R-project.org/package=cluster>.
 40. Kassambara A, Mundt F. factoextra: Extract and Visualize the Results of Multivariate Data Analyses. R Package Version 1.0.7. 2020. <https://CRAN.R-project.org/package=factoextra>.
 41. Henningsen A, Toomet O. miscTools: Miscellaneous Tools and Utilities. R Package Version 0.6-28. 2023. <https://cran.r-project.org/web/packages/miscTools/>.
 42. Kuhn M. Building predictive models in R using the caret package. *J Stat Softw.* 2008;28(5):1–26. <https://doi.org/10.18637/jss.v028.i05>.
 43. Jang EH, Lee JH, Kim SA. Acute valproate exposure induces mitochondrial biogenesis and autophagy with foxo3a modulation in sh-sy5y cells. *Cells.* 2021;10(10). <https://doi.org/10.3390/cells10102522>
 44. Ashley N, O'Rourke A, Smith C, et al. Depletion of mitochondrial DNA in fibroblast cultures from patients with POLG1 mutations is a consequence of catalytic mutations. *Hum Mol Genet.* 2009;18(24):4905–6. <https://doi.org/10.1093/hmg/ddp458>.
 45. Park KS, Jo I, Pak Y, et al. FCCP depolarizes plasma membrane potential by activating proton and Na⁺ currents in bovine aortic endothelial cells. *Pflugers Arch.* 2002;443(3):344–52. <https://doi.org/10.1007/s004240100703>.
 46. Bakare AB, Daniel J, Stabach J, et al. Quantifying mitochondrial dynamics in patient fibroblasts with multiple developmental defects and mitochondrial disorders. *Int J Mol Sci.* 2021;22(12). <https://doi.org/10.3390/ijms22126263>
 47. Distelmaier F, Koopman WJH, Van Den Heuvel LP, et al. Mitochondrial complex I deficiency: From organelle dysfunction to clinical disease. *Brain.* 2009;132(4):833–42. <https://doi.org/10.1093/brain/awp058>.
 48. Pugsley HR. Assessing Autophagic Flux by Measuring LC3, p62, and LAMP1 Co-localization Using Multispectral Imaging Flow Cytometry. *J Vis Exp.* 2017;125:55637. <https://doi.org/10.3791/55637>.
 49. Cullup T, Kho AL, Dionisi-Vici C, et al. Recessive mutations in EPG5 cause Vici syndrome, a multisystem disorder with defective autophagy. *Nat Genet.* 2013;45(1):83–7. <https://doi.org/10.1038/ng.2497>.
 50. Di Pietro N, Marcovecchio ML, Di Silvestre S, et al. Plasma from pre-pubertal obese children impairs insulin stimulated Nitric Oxide (NO)

- bioavailability in endothelial cells: Role of ER stress. *Mol Cell Endocrinol*. 2017;443:52–62. <https://doi.org/10.1016/j.mce.2017.01.001>.
51. Rita Lecca M, Wagner U, Patrignani A, Berger EG, Hennes T. Genome-wide analysis of the unfolded protein response in fibroblasts from congenital disorders of glycosylation type-I patients. *FASEB J*. 2005;19(2):1–21. <https://doi.org/10.1096/fj.04-2397fje>.
 52. Wortzel I, Koifman G, Rotter V, Seeger R, Porat Z. High Throughput Analysis of Golgi Structure by Imaging Flow Cytometry. *Sci Rep*. 2017;7(1):788. <https://doi.org/10.1038/s41598-017-00909-y>.
 53. Scrivens PJ, Shahrzad N, Moores A, Morin A, Brunet S, Sacher M. TRAP-PC2L is a novel, highly conserved TRAPP-interacting protein. *Traffic*. 2009;10(6):724–36. <https://doi.org/10.1111/j.1600-0854.2009.00906.x>.
 54. George TC, Fanning SL, Fitzgerald-Bocarsly P, et al. Quantitative measurement of nuclear translocation events using similarity analysis of multispectral cellular images obtained in flow. *J Immunol Methods*. 2006;311(1–2):17–29. <https://doi.org/10.1016/j.jim.2006.01.018>.
 55. Mandola AB, Sharfe N, Nagdi Z, et al. Combined immunodeficiency caused by a novel homozygous NFKB1 mutation. *Journal of Allergy and Clinical Immunology*. 2021;147(2):727–733.e2. <https://doi.org/10.1016/j.jaci.2020.08.040>.
 56. Rajan R, Karbowiczek M, Pugsley HR, Sabnani MK, Astrinidis A, La-Beck NM. Quantifying autophagosomes and autolysosomes in cells using imaging flow cytometry. *Cytometry A*. 2015;87(5):451–8. <https://doi.org/10.1002/cyto.a.22652>.
 57. Ratinaud MH, Lepret P, Julien R. In situ flow cytometric analysis of nonyl acridine orange-stained mitochondria from splenocytes. *Cytometry*. 1988;9(3):206–12. <https://doi.org/10.1002/cyto.990090304>.
 58. Creed S, McKenzie M. Measurement of mitochondrial membrane potential with the fluorescent dye tetramethylrhodamine methyl ester (TMRM). *Methods Mol Biol*. 2019;1928:69–76. https://doi.org/10.1007/978-1-4939-9027-6_5.
 59. de Jesús TJ, Ramakrishnan P. NF- κ B c-Rel Dictates the Inflammatory Threshold by Acting as a Transcriptional Repressor. *iScience*. 2020;23(3):100876. <https://doi.org/10.1016/j.isci.2020.100876>.
 60. Gottschalk RA, Martins AJ, Angermann BR, et al. Distinct NF- κ B and MAPK Activation Thresholds Uncouple Steady-State Microbe Sensing from Antipathogen Inflammatory Responses. *Cell Syst*. 2016;2(6):378–90. <https://doi.org/10.1016/j.cels.2016.04.016>.
 61. Dai C, Dai S, Cao J. Proteotoxic stress of cancer: Implication of the heat-shock response in oncogenesis. *J Cell Physiol*. 2012;227(8):2982–7. <https://doi.org/10.1002/jcp.24017>.
 62. Morán M, Delmiro A, Blázquez A, Ugalde C, Arenas J, Martín MA. Bulk autophagy, but not mitophagy, is increased in cellular model of mitochondrial disease. *Biochim Biophys Acta Mol Basis Dis*. 2014;1842(7):1059–70. <https://doi.org/10.1016/j.bbadis.2014.03.013>.
 63. Ghosh AK, Mau T, O'Brien M, Garg S, Yung R. Impaired autophagy activity is linked to elevated ER-stress and inflammation in aging adipose tissue. *Aging*. 2016;8(10):2525–37. <https://doi.org/10.18632/aging.101083>.
 64. Karkucinska-Wieckowska A, Trubicka J, Werner B, et al. Left ventricular noncompaction (LVNC) and low mitochondrial membrane potential are specific for Barth syndrome. *J Inher Metab Dis*. 2013;36(6):929–37. <https://doi.org/10.1007/s10545-013-9584-4>.
 65. Anderson GW, Goebel HH, Simonati A. Human pathology in NCL. *Biochimica et Biophysica Acta (BBA) - Molecular Basis of Disease*. 2013;1832(11):1807–1826. <https://doi.org/10.1016/j.bbadis.2012.11.014>.
 66. Anderson G, Smith VV, Malone M, Sebire NJ. Blood film examination for vacuolated lymphocytes in the diagnosis of metabolic disorders; retrospective experience of more than 2500 cases from a single centre. *J Clin Pathol*. 2005;58(12):1305–10. <https://doi.org/10.1136/jcp.2005.027045>.
 67. Aula P, Rapola J, Andersson LC. Distribution of cytoplasmic vacuoles in blood T and B lymphocytes in two lysosomal disorders. *Virchows Arch B Cell Pathol*. 1975;18(1):263–71. <https://doi.org/10.1007/BF02889252>.
 68. Schiff M, Haberberger B, Xia C, et al. Complex I assembly function and fatty acid oxidation enzyme activity of ACAD9 both contribute to disease severity in ACAD9 deficiency. *Hum Mol Genet*. 2014;24(11):3238–47. <https://doi.org/10.1093/hmg/ddv074>.
 69. Nasca A, Nardecchia F, Commone A, et al. Clinical and Biochemical Features in a Patient With Mitochondrial Fission Factor Gene Alteration. *Front Genet*. 2018;9. <https://doi.org/10.3389/fgene.2018.00625>.
 70. Passmore JB, Carmichael RE, Schrader TA, et al. Mitochondrial fission factor (MFF) is a critical regulator of peroxisome maturation. *Biochimica et Biophysica Acta (BBA) - Molecular Cell Research*. 2020;1867(7):118709. <https://doi.org/10.1016/j.bbamcr.2020.118709>.
 71. Schrader TA, Carmichael RE, Islinger M, et al. PEX11 β and FIS1 cooperate in peroxisome division independently of mitochondrial fission factor. *J Cell Sci*. 2022;135(13). <https://doi.org/10.1242/jcs.259924>.
 72. Shamseldin HE, Alshammari M, Al-Sheddi T, et al. Genomic analysis of mitochondrial diseases in a consanguineous population reveals novel candidate disease genes. *J Med Genet*. 2012;49(4):234–41. <https://doi.org/10.1136/jmedgenet-2012-100836>.
 73. D'Alessandro G, Morales-Juarez DA, Richards SL, et al. RAD54L2 counters TOP2-DNA adducts to promote genome stability. *Sci Adv*. 2023;9(49):eadl2108. <https://doi.org/10.1126/sciadv.adl2108>.
 74. Haralick R, Shanmugam K, Its'hak D. Textural features for image classification. *IEEE Trans Syst Man Cybern*. 1993;6:10–21.
 75. Zhang H, Xiong Y, Sun Y, et al. RAD54L2-mediated DNA damage avoidance pathway specifically preserves genome integrity in response to topoisomerase 2 poisons. *Sci Adv*. 2023;9(49). <https://doi.org/10.1126/sciadv.adl6681>.
 76. Chen S, Francioli LC, Goodrich JK, et al. A genomic mutational constraint map using variation in 76,156 human genomes. *Nature*. 2024;625(7993):92–100. <https://doi.org/10.1038/s41586-023-06045-0>.
 77. Schwarz JM, Rödelsperger C, Schuelke M, Seelow D. MutationTaster evaluates disease-causing potential of sequence alterations. *Nat Methods*. 2010;7(8):575–6. <https://doi.org/10.1038/nmeth0810-575>.
 78. Milanese C, Bombardieri CR, Sepe S, et al. DNA damage and transcription stress cause ATP-mediated redesign of metabolism and potentiation of anti-oxidant buffering. *Nat Commun*. 2019;10(1). <https://doi.org/10.1038/s41467-019-12640-5>.
 79. De Waard MC, Van Der Pluijm I, Zuiderveen Borgesius N, et al. Age-related motor neuron degeneration in DNA repair-deficient *Erc1* mice. *Acta Neuropathol*. 2010;120(4):461–75. <https://doi.org/10.1007/s00401-010-0715-9>.
 80. De Voer RM, Hahn MM, Mensenkamp AR, et al. Deleterious Germline BLM mutations and the risk for early-onset colorectal cancer. *Sci Rep*. 2015;5. <https://doi.org/10.1038/srep14060>.
 81. Dregalla RC, Zhou J, Idate RR, Battaglia CLR, Liber HL, Bailey SM. Regulatory roles of tankyrase 1 at telomeres and in DNA repair: Suppression of T-SCE and stabilization of DNA-pkcs. *Aging*. 2010;2(10):691–708. <https://doi.org/10.18632/aging.100210>.
 82. Kaji N, Muramoto A, Mizuno K. LIM kinase-mediated cofilin phosphorylation during mitosis is required for precise spindle positioning. *J Biol Chem*. 2008;283(8):4983–92. <https://doi.org/10.1074/jbc.M708644200>.
 83. Chao JT, Hollman R, Meyers WM, Meili F, Matreyek KA, Dean P, et al. A premalignant cell-based model for functionalization and classification of PTEN variants. *Cancer Res*. 2020;80(13):2775–89. <https://doi.org/10.1158/0008-5472.CAN-19-3278>.
 84. Ebrahimi-Fakhari D, Alecu JE, Brechmann B, et al. High-throughput imaging of ATG9A distribution as a diagnostic functional assay for adaptor protein complex 4-associated hereditary spastic paraplegia. *Brain Commun*. 2021;3(4). <https://doi.org/10.1093/braincomms/fcab221>.
 85. Caicedo JC, Arevalo J, Piccioni F, et al. Cell Painting predicts impact of lung cancer variants. *Mol Biol Cell*. 2022;33(6). <https://doi.org/10.1091/mbc.E21-11-0538>.
 86. Ohya Y, Sese J, Yukawa M, et al. High-dimensional and large-scale phenotyping of yeast mutants. *Proc Natl Acad Sci U S A*. 2005;102(52):19015–20. <https://doi.org/10.1073/pnas.0509436102>.
 87. Matreyek KA, Starita LM, Stephany JJ, et al. Multiplex assessment of protein variant abundance by massively parallel sequencing. *Nat Genet*. 2018;50(6):874–82. <https://doi.org/10.1038/s41588-018-0122-z>.
 88. Weile J, Roth FP. Multiplexed assays of variant effects contribute to a growing genotype-phenotype atlas. *Hum Genet*. 2018;137(9):665–78. <https://doi.org/10.1007/s00439-018-1916-x>.
 89. Gasperini M, Starita L, Shendure J. The power of multiplexed functional analysis of genetic variants. *Nat Protoc*. 2016;11(10):1782–7. <https://doi.org/10.1038/nprot.2016.135>.
 90. Chowdhury A, Aich A, Jain G, et al. Defective Mitochondrial Cardiolipin Remodeling Dampens HIF-1 α Expression in Hypoxia. *Cell Rep*. 2018;25(3):561–570.e6. <https://doi.org/10.1016/j.celrep.2018.09.057>.
 91. Zemirli N, Pourcelot M, Ambroise G, Hachi E, Vazquez A, Arnoult D. Mitochondrial hyperfusion promotes NF- κ B activation via the mitochondrial

E3 ligase MULAN. *FEBS J.* 2014;281(14):3095–112. <https://doi.org/10.1111/febs.12846>.

92. Unzueta-Larrinaga P, Barrena-Barbadillo R, Ibarra-Lecue I, et al. Isolation and Differentiation of Neurons and Glial Cells from Olfactory Epithelium in Living Subjects. *Mol Neurobiol.* 2023;60(8):4472–87. <https://doi.org/10.1007/s12035-023-03363-2>.
93. Irena Josephina Johanna Muffels. SCV005387562. ClinVar. 2024. Accessed December 23, 2024. [https://www.ncbi.nlm.nih.gov/clinvar/variation/3374700/?oq=SCV005387562&m=NM_015106.4\(RAD54L2\):c.389A%3EG%20\(p.Gln130Arg\)](https://www.ncbi.nlm.nih.gov/clinvar/variation/3374700/?oq=SCV005387562&m=NM_015106.4(RAD54L2):c.389A%3EG%20(p.Gln130Arg))

Publisher's Note

Springer Nature remains neutral with regard to jurisdictional claims in published maps and institutional affiliations.